

**Development of Ultrafiltration Titanium Dioxide  
Magnéli Phase Reactive Electrochemical Membranes**

BY

Lun Guo

B.S. University of Michigan, Ann Arbor, 2012

B.S. Shanghai Jiao Tong University, 2013

THESIS

Submitted as partial fulfillment of the requirements  
for the degree of Master of Science in Chemical Engineering  
in the Graduate College of the  
University of Illinois at Chicago, 2015

Chicago, Illinois

Defense Committee:

Brian P. Chaplin, Chair and Advisor

Vivek Sharma

Lewis E. Wedgewood

This thesis is dedicated to my wife, Yuchen Tang, without whom it would never have been accomplished.

## **ACKNOWLEDGMENTS**

I would like to thank my advisor—Prof. Brian P. Chaplin for his unwavering support and assistance. He provided guidance in all areas that helped me accomplish my research goals and enjoy myself in the process.

LG

## TABLE OF CONTENTS

Chapter I: INTRODUCTION .....	1
Chapter II: LITERATURE REVIEW .....	4
A. Titanium Oxide Magnéli Phase .....	4
B. Electrochemical Advanced Oxidation Processes .....	4
C. Electrochemical Membrane Filtration .....	8
D. Treatment for Nitrate .....	10
Chapter III: MATERIALS AND METHODS.....	13
A. Material .....	13
B. Reactive Electrochemical Membrane Synthesis. ....	13
C. Membrane Characterization. ....	13
D. Cross-flow Filtration Setup. ....	14
E. Cross Flow Filtration Experiment .....	15
F. Analytical Method .....	17
Chapter IV: RESULT AND DISCUSSION .....	19
A. Physical Characterization. ....	19
B. Reactivity Characterization. ....	22
C. Electrochemical Oxidation of Oxalic Acid. ....	25
D. Hydroxyl Radical Probe Studies. ....	28
E. Electrochemical Separation of Oxyanions. ....	30
Chapter V: CONCLUSIONS .....	36
APPENDICES .....	38
A. Hg Porosimetry.....	38
B. Permeate Flux.....	39
C. EIS Measurement of Electroactive Surface Area .....	40
D. Oxyanion Separation .....	42
E. Energy Consumption Estimation (Electrolyte) .....	45
F. Hydroxyl Radical Probe (Duplicates Experiments) .....	46
G. Energy Consumption Estimations (NaNO <sub>3</sub> ).....	47
REFERENCE.....	48
VITA .....	59

## LIST OF TABLES

TABLE I. SUMMARY OF DATA FOR OXYANION SEPARATION.....	32
---	----

## LIST OF FIGURES

<b>Figure 1.</b> XRD and SEM data for membrane characterization. ....	21
<b>Figure 2.</b> Observed kinetic rate constant plot .....	23
<b>Figure 3.</b> Direct electron transfer test with oxalic acid .....	28
<b>Figure 4.</b> Hydroxyl radical test with coumarin and terephthalic acid .....	30
<b>Figure 5.</b> Oxyanion separation with electrostatic and prediction of ion concentration .....	31
<b>Figure 6.</b> Hg porosimetry analysis of cumulative pore area and pore volume .....	38
<b>Figure 7.</b> Pressure-normalized permeate membrane flux profiles for REM.....	39
<b>Figure 8.</b> Measured EIS data for REM-3 .....	41
<b>Figure 9.</b> Comparison of experimental measurements of $u$ versus the pressure drop. ....	44
<b>Figure 10.</b> Polarization curves with $\text{NaClO}_4$ solution at varied flux.....	45
<b>Figure 11.</b> Repeated experiment for hydroxyl radical test .....	46
<b>Figure 12.</b> Polarization curves with $\text{NaNO}_3$ solution.....	47

## LIST OF ABBREVIATIONS

COU	Coumarin
EAOP	Electrochemical Advanced Oxidation Process
ED	Electro Dialysis
EIS	Electrochemical Impedance Spectroscopy
HTA	2-Hydroxyterephthalic Acid
IE	Ion Exchange
OA	Oxalic Acid
OH•	Hydroxyl Radical
REM	Reactive Electrochemical Membrane
RO	Reverse Osmosis
SEM	Scanning Electron Microscopy
TA	Terephthalic Acid
TLM	Transmission Line Model
XRD	X-ray Diffraction

## Summary

This research focused on the synthesis, characterization, and performance testing of a novel Magnéli phase ( $\text{Ti}_n\text{O}_{2n-1}$ ),  $n = 4$  to  $6$ , reactive electrochemical membrane (REM) for water treatment. The REMs were synthesized from tubular asymmetric  $\text{TiO}_2$  ultrafiltration membranes, and optimal reactivity was achieved for REMs comprised of high purity  $\text{Ti}_4\text{O}_7$ . Probe molecules were used to assess outer-sphere charge transfer ( $\text{Fe}(\text{CN})_6^{4-}$ ) and organic compound oxidation through both direct oxidation (oxalic acid) and formation of  $\text{OH}^\bullet$  (coumarin, terephthalic acid). High membrane fluxes ( $3208 \text{ L m}^{-2} \text{ hr}^{-1} \text{ bar}^{-1}$  (LMH  $\text{bar}^{-1}$ )) were achieved and resulted in a convection-enhanced rate constant for  $\text{Fe}(\text{CN})_6^{4-}$  oxidation of  $1.4 \times 10^{-4} \text{ m s}^{-1}$ , which is the highest reported in an electrochemical flow-through reactor and approached the kinetic limit. The optimal removal rate for oxalic acid was  $401.5 \pm 18.1 \text{ mmole h}^{-1} \text{ m}^{-2}$  at 793 LMH, with approximately 84% current efficiency. Experiments indicate  $\text{OH}^\bullet$  were produced only on the  $\text{Ti}_4\text{O}_7$  REM, and not on less reduced phases (e.g.,  $\text{Ti}_6\text{O}_{11}$ ). REMs were also tested for oxyanion separation. Approximately 67% removal of a 1 mM  $\text{NO}_3^-$  solution was achieved at 58 LMH, with energy consumption of  $0.22 \text{ kWh m}^{-3}$ . These results demonstrate the extreme promise of REMs for water treatment applications.



## Chapter I: INTRODUCTION

Reactive electrochemical membranes (REMs) are a promising technology that combines an electrochemical advanced oxidation process (EAOP) and physical separation into a single water treatment device. EAOP is the process by which water is oxidized on an anode surface to form hydroxyl radicals ( $\text{OH}^\bullet$ ), which react with a wide range of recalcitrant organic and inorganic compounds often at diffusion-controlled rates.<sup>1</sup> Magnéli phase titanium oxides ( $\text{Ti}_n\text{O}_{2n-1}$ ),  $n = 4$  to  $10$ , have been utilized for REM fabrication because they can be synthesized into porous monolithic structures at low cost and are reported to produce  $\text{OH}^\bullet$  via water oxidation.<sup>2,3</sup> The unique chemical, electrical, and magnetic properties of  $\text{Ti}_n\text{O}_{2n-1}$  have motivated their use as battery electrodes,<sup>4-6</sup> fuel cell supports,<sup>6,7</sup> memristor devices,<sup>8,9</sup> photocatalysts,<sup>10</sup> and electrodes for electrochemical oxidation,<sup>11,12</sup> and reduction<sup>6,13,14</sup> of water contaminants.

The seminal work by Zaky and Chaplin demonstrated that commercial, tubular  $\text{Ti}_n\text{O}_{2n-1}$  monolithic electrodes (Ebonex®) could be utilized as REMs for the oxidation of several organic compounds at high current efficiencies.<sup>3</sup> Results showed that reaction rates were limited by convection to the REM, due to the fast radial diffusion of compounds in the micron-sized REM pores.<sup>3</sup> These promising results suggest that reaction rates can be increased by simply increasing the permeate flux and that intrinsic reaction rates of the electrode should be obtained at sufficiently high fluxes. However, the Ebonex REM pore structure was not tailored for water treatment, which resulted in a high-pressure drop across the membrane and thus low pressure-normalized permeate fluxes (e.g.,  $50\text{-}70 \text{ L m}^{-2} \text{ hr}^{-1} \text{ bar}^{-1}$

(LMH bar<sup>-1</sup>)).<sup>2,3</sup> Additionally, Ebonex electrodes often contain a range of Magnéli phases (n = 4 to 10),<sup>15</sup> which can affect electrode conductivity and presumably EAOP performance. While it is well known that Ti<sub>4</sub>O<sub>7</sub> is the most conductive Magnéli phase suboxide (e.g., 20,000-100,000 S m<sup>-1</sup>),<sup>6,15</sup> studies focused on providing a link between Magnéli phase composition and EAOP performance are lacking.

Another unexplored area of research for REMs is their use as electrostatic barriers for ion separation. Related technologies, such as carbon nanotube-polymer composite membranes,<sup>16,17</sup> have shown the ability to reduce membrane fouling due to electrostatic repulsion of negatively charged organics at cathodically polarized membrane surfaces. However, to our knowledge work focused on ion separation by an electrically conductive membrane has not been reported. Although electro dialysis (ED) is similar in function, the technology is fundamentally different from REMs. ED membranes possess high ionic conductivity but are electrically insulating. Polymeric ED membranes suffer from high production costs, are susceptible to organic and mineral fouling, and are not chemically robust, which increase the capital costs and operation and maintenance costs for ED water treatment.<sup>18</sup>

The focus of this work is on the synthesis and testing of a novel REM that is applied to water treatment. The REM is synthesized from an asymmetric TiO<sub>2</sub> ultrafiltration membrane to produce a conductive Ti<sub>n</sub>O<sub>2n-1</sub> membrane with high liquid flux and minimal pressure drop. The REM is characterized by scanning electron microscopy (SEM), X-ray diffraction (XRD), electrochemical impedance spectroscopy (EIS), and Hg porosimetry. The effect of the Magnéli phase composition on electrode conductivity, charge transfer, and OH<sup>•</sup> generation is

explored. Additionally, the utility of the REM for organic compound oxidation and electrostatic separation of toxic oxyanions (e.g.,  $\text{NO}_3^-$  and  $\text{ClO}_4^-$ ) is demonstrated.

## Chapter II. LITERATURE REVIEW

### A. Titanium Oxide Magnéli Phase

Ceramic Magnéli phase titanium oxides materials ( $\text{Ti}_n\text{O}_{2n-1}$ ),  $n = 4$  to  $10$ , have been attracting attention since the 1990s. The reported conductivity of Magnéli phase titanium oxides ranges from  $25$  to  $1995 \text{ S cm}^{-1}$ ,<sup>6,19</sup> and among them,  $\text{Ti}_4\text{O}_7$  is the most conductive, chemically inert, and corrosion resistive Magnéli phase.<sup>15</sup> Also, the reactivity towards both inorganic and organic compounds is high.<sup>3,14</sup> Due to the unique thermal stability, high electrochemical reactivity and corrosion resistance, Magnéli phase materials have been used as electrodes (batteries<sup>4-6</sup>, oxidation<sup>11,12</sup> and reduction<sup>6,13,14</sup> in water treatment), fuel cell supports,<sup>6,7</sup> memristor devices,<sup>8,9</sup> and photocatalysts.<sup>10</sup>

The Magnéli phase material is obtained by sintering at high temperature ( $850^\circ\text{C}$  to  $1300^\circ\text{C}$ ) in a reductive environment, such as  $\text{H}_2$ ,<sup>20</sup>  $\text{NH}_3$ ,<sup>21</sup> zirconium,<sup>22</sup> or carbon.<sup>23</sup> The reduction reaction creates oxygen deficiencies with prolonged reduction time, which produces an n-type doped structure and imparts electrical conductivity.

### B. Electrochemical Advanced Oxidation Processes

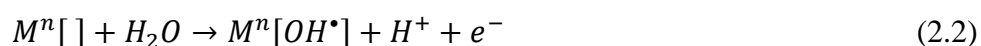
Treatment of organic matter in wastewater is important, and existing methods include biological treatment, chemical oxidation, advanced oxidation processes (AOPs), and electrochemical advanced oxidation processes (EAOPs). Biological treatment is cheapest among those methods, but the toxic and biorefractory contaminations in water may hinder the treatment process. Treatment using chemical oxidation may generate toxic byproducts which may be more harmful than the initial contaminants.<sup>24</sup> Another oxidation technique, known as

advanced oxidation processes (AOPs), is used to remove pollutants by producing hydroxyl radicals ( $\text{OH}^\bullet$ ). The  $\text{OH}^\bullet$  is one of the strongest oxidants and can destroy a wide range of recalcitrant organic compounds. AOPs can be categorized as dark AOPs (e.g., Ozone/catalyst, Ozone at elevated pH and Fenton process) and photo-assisted AOPs (e.g., Ozone/UV,  $\text{H}_2\text{O}_2$ /UV,  $\text{TiO}_2$ /UV and etc.).<sup>25</sup> In general AOPs are cheap to install, but the operational costs are expensive (\$0.03 to \$43.46  $\text{L}^{-1}$ ),<sup>26</sup> due to the usage of costly chemicals like  $\text{H}_2\text{O}_2$  and high consumption of energy.<sup>27</sup> Another disadvantage of AOPs is that the efficiency is decreased in natural water because of  $\text{OH}^\bullet$  scavenging by natural organic matter and carbonate species.<sup>28</sup>

The electrochemical advanced oxidation process (EAOP) is a new technology developed for the treatment of contaminated water. Similar to the AOPs, EAOPs are also based on the production of  $\text{OH}^\bullet$ , but via an electrochemical pathway. The generation of  $\text{OH}^\bullet$  on the electrode surface by the oxidation of water is shown in the following equation:



The anode electrode materials used for EAOPs include doped- $\text{SnO}_2$ ,  $\text{PbO}_2$  and doped- $\text{PbO}_2$ , and boron-doped diamond (BDD).<sup>12</sup> These electrode materials have a common feature in that they have a high overpotential for electrochemical  $\text{O}_2$  production ( $\sim 2$  V vs. the standard hydrogen electrode (SHE)), which allows the generation of  $\text{OH}^\bullet$  to take occur instead of O atom pairing and  $\text{O}_2$  production.<sup>12</sup> Additionally, the aforementioned electrodes are classified as inactive electrodes. For these kind of materials, the oxidation state do not change during the oxidation experiments. The equation below shows an example of  $\text{OH}^\bullet$  generation of at an inactive electrode surface:<sup>12,29</sup>



The electrode surface site  $M^n[ ]$  is in oxidation state “n” during the whole oxidation process, and the weak adsorption between  $OH^\bullet$  and the electrode surface site allows them to be available to react with organic compounds near the electrode surface. By contrast, active electrodes are oxidized to a higher oxidation state during the water oxidation process as shown below:<sup>12,29</sup>



For this reason, the  $OH^\bullet$  generation at active electrodes is much less than that on inactive electrode, and the oxidation processes occurs shown as following:<sup>12,29</sup>



The inactive electrodes mentioned above (doped-SnO<sub>2</sub>, PbO<sub>2</sub> and doped-PbO<sub>2</sub>, and BDD) are the most effective for EAOPs; yet there are some disadvantages with these materials. The doped-SnO<sub>2</sub> is often doped with Sb. The doping process increases conductivity of the electrode and allows it to function as an EAOP; however, Sb is toxic and regulated by the EPA at a concentration of 6 µg L<sup>-1</sup> in drinking water sources.<sup>30</sup> There are also studies on doped-SnO<sub>2</sub> electrodes using other dopants (e.g., Ar), but the serve life is short.<sup>12</sup> Studies using PbO<sub>2</sub> electrodes have confirmed the electrochemical generation of  $OH^\bullet$ , and the oxidation efficiency is close to that of BDD electrodes, which are considered to be the most active electrode material.<sup>31</sup> Doped-PbO<sub>2</sub> electrodes have even higher electrochemical activity than that of PbO<sub>2</sub> electrodes. Both PbO<sub>2</sub> and doped-PbO<sub>2</sub> electrodes are stable during oxidation experiments, and minimal leaching has been documented.<sup>32</sup> However, there is still concern over the potential for slow leaching of Pb during the treatment process.

The BDD electrodes are the most promising and widely used for EAOPs, and they are

commercially available. For example, dedicated products using BDD electrodes like Oxineo® and Sysneo® have been developed for disinfection of swimming pools. These systems using EAOPs have several advantages over other disinfection methods, such as the absence of chlorine odor and the systems do not require any chemical addition. BDD has several advantages including high electrochemical activity and stability during anodic polarization. However, the BDD film electrodes have a disadvantage of the film delamination from the substrates.<sup>33</sup> The traditional substrate for BDD electrodes, p-silicon, is able to prevent film delamination, but it is not suitable for industrial applications due to the fragility of Si.

Another promising, but seldom used, electrode for EAOPs is doped- and sub-stoichiometric TiO<sub>2</sub>. Titanium dioxide is widely used in products like paint, paper, and ink, and costs approximately \$3,300 – \$3,500 per ton.<sup>34</sup> Stoichiometric TiO<sub>2</sub> is nonconductive, but the conductivity can be drastically increased by creating oxygen deficiencies or doping with Nb. Ti<sub>4</sub>O<sub>7</sub> is one of the most conductive and active of the Magnéli phases, with an electrical conductivity of 166 S cm<sup>-1</sup>.<sup>15</sup> Studies have shown that Ti<sub>4</sub>O<sub>7</sub> is highly corrosion resistant and electrochemically stable.<sup>15</sup> Commercially available Magnéli phase ceramic electrodes, known as Ebonex®, have shown comparable electrochemical reactivity to BDD.<sup>35</sup> However, studies have shown that a passivating TiO<sub>2</sub> coating is formed during anodic polarization.<sup>36,37</sup> Some studies reported that the passivation layer is not reversible,<sup>37</sup> but others report that the passivation is reversible under cathodic polarization.<sup>38</sup> The exact mechanism of passivation/reactivation of Ti<sub>4</sub>O<sub>7</sub> electrodes is not clear and further studies are needed.

One possible solution to the passivation problem is to dope  $\text{TiO}_2$  with Nb. Doping  $\text{TiO}_2$  with Nb, known as Niobium-doped rutile (NDR), results in very high conductivity ( $0.2\text{--}1.5\text{ S cm}^{-1}$ ).<sup>12,36,39</sup> NDR electrodes have been utilized in regenerative fuel cells, and have a promising applications for many other technologies.<sup>12</sup>  $\text{Ti}_4\text{O}_7$  and NDR are both promising for water treatment, but few studies on these materials are published.

### **C. Electrochemical Membrane Filtration**

Ultrafiltration (UF) is a promising technology for drinking water treatment. The utilization of membrane filtration can simplify and even eliminate several steps (e.g., coagulation, sedimentation, and granular filtration) in water treatment process. There are several advantages of membrane filtration, such as high product water quality, compact modular design, small footprint, as well as stable and high performance in handling large fluctuations in feed water compositions.<sup>40</sup> Thus, ultrafiltration membrane systems are widely utilized for drinking water treatment all over the world.<sup>41,42</sup> However, membrane fouling caused by accumulation of organic and inorganic materials on the membrane surface results in increased power consumption and reduced membrane lifetime.

Several methods are proposed to reduce membrane fouling by modification of the membrane surface. One way is the utilization of UF membrane additives (e.g.,  $\text{Al}_2\text{O}_3$ ,  $\text{TiO}_2$ , nanoparticles, and organic copolymers)<sup>16</sup> to create a more hydrophilic surface. The hydrophilic surface favors water adsorption, and hinders adsorption of organic matter. Alternatively, increasing the negative surface charge density of the UF membrane surface can reduce fouling via charge repulsion.<sup>43</sup> However, this method can further complicate the fouling process because certain functional groups, like carboxylates, form calcium ion



bridges between the organic matter and membrane surface. These ion bridges reduce permeability and decrease the reversibility of fouling.<sup>44</sup>

An alternative method to modify the membrane surface is to introduce negative charge via applying a potential on conductive ultrafiltration membranes. This type of membrane is known as electro-filtration membranes. Examples of proposed materials for current-carrying membranes are conductive polymers and carbon nanotubes (CNT).<sup>45</sup> However, the conductive polymer membranes can suffer from low permeability, low stability, poor separation characteristics, and brittleness.<sup>46</sup> Carbon nanotubes (CNTs) are proposed as conductive materials for membranes because of their high electrical conductivity.<sup>47</sup> Conductive membranes like polymer-multiwalled carbon nanotube nanocomposite membranes<sup>45</sup> and carbon nanotube-polyvinylidene fluoride (CNT-PVDF) membranes<sup>16</sup> are synthesized with CNTs and polymers. By cathodically polarization of the membrane surface, these composite membranes can reduce fouling by electrostatic repulsion of negatively charged organics.<sup>16,45</sup> Besides the application on reducing fouling, the membrane comprised by conductive materials (e.g. graphene-CNT,<sup>48</sup> CNT stack,<sup>49</sup> and CNT-PVDF<sup>50</sup>) can also be used for removal of organic wastes.

Another promising material for UF membranes is sub-stoichiometric TiO<sub>2</sub>. This type of material is stable under both anodic and cathodic polarization, chemically inert, and highly reactive with both inorganic and organic compounds in wastewater.<sup>3,12,15</sup> Previously, Zaky and Chaplin<sup>2,3</sup> tested a reactive electrochemical membrane (REM) comprised of Ebonex Magnéli phase materials. It was shown that the REM could integrate membrane filtration and EAOPs, as they combined the advantages of both technologies into a single electrochemical

device. The REM used by Zaky and Chaplin is not suited for ultrafiltration due to the large trans-membrane pressure drop and thus low pressure-normalized permeate flux.<sup>3</sup> This disadvantage will result in large operation cost and high energy consumption during drinking water treatment processes. However, with modification of the porous structure, the TiO<sub>2</sub> Magnéli phase material has promise as an ultrafiltration membrane for drinking water treatment. Few studies on fouling with this type of ultrafiltration membrane are found, and this area needs to be further studied.

#### **D. Treatment for Nitrate**

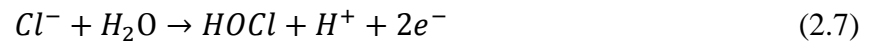
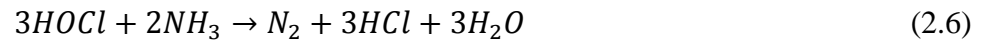
Nitrate (NO<sub>3</sub><sup>-</sup>) is the most widespread contaminant in the world. The sources of NO<sub>3</sub><sup>-</sup> in drinking water sources are from fertilizer use, leaking from septic tanks, and erosion of natural deposits.<sup>30</sup> The EPA has regulated NO<sub>3</sub><sup>-</sup> in drinking water at a maximum contaminant level (MCL) of 10 mg L<sup>-1</sup> as N. Drinking water containing NO<sub>3</sub><sup>-</sup> concentration exceeding the MCL will cause serious illness for infants, like shortness of breath, methemoglobinemia, and even death.<sup>30</sup> To remove NO<sub>3</sub><sup>-</sup> in drinking water, catalytic NO<sub>3</sub><sup>-</sup> reduction has been developed since the 1980s, and uses typical catalyst like Pd-Cu, Pd-In, and Pd-Sn. The reduction of NO<sub>3</sub><sup>-</sup> results in production of N<sub>2</sub> and other byproducts such as NH<sub>3</sub>, NO<sub>2</sub><sup>-</sup>, NO, and N<sub>2</sub>O.<sup>51</sup> Other methods of NO<sub>3</sub><sup>-</sup> removal include electro dialysis (ED), reverse osmosis (RO), and ion exchange (IE). Both ED and RO have been proven to be reliable, efficient and require minimal chemical usage.<sup>52</sup> However, RO is nonselective, and any molecules larger than the size of water will be rejected from the water stream. The costs for both ED and RO are high, and extra cost for membrane replacement has to be considered.<sup>18,52</sup>

Cost estimates for nitrate removal by ED are limited due to the existence of only few

full-scale systems. However, reports by General Electric indicate that the capital cost for ED systems is \$1.11 per gallon, and operation cost is \$2.09 per 1000 gallons.<sup>53</sup> The cost for RO highly depends on the amount of water recovery. The estimates given by GE show that the total annualized cost per 1000 gallons for treated water is from \$2.52 to \$19.70.<sup>53</sup> The IE process is the most suitable method when providing drinking water in small volumes as it is simple, effective, selective, and inexpensive.<sup>54</sup> The annualized cost of IE process is from \$0.5 to \$2.19 per 1000 gallons.<sup>53</sup>

Electrochemical reduction of  $\text{NO}_3^-$  has been researched using different cathodes. Reported cathode materials that have been used for electrochemical  $\text{NO}_3^-$  reduction are Sn,<sup>55</sup> Cu,<sup>56</sup> Cu-Zn,<sup>57,58</sup> Cu-Sn,<sup>58</sup> Cu-Ru,<sup>59</sup> Ir-Pt,<sup>60</sup> Sn modified Pt/Ti,<sup>61</sup> Bi modified Pt,<sup>62</sup>  $\text{Cu}^{2+}$ - and  $\text{Ni}^{2+}$ -containing Dawson-type polyoxometalates,<sup>63</sup> Cu-Pd modified BDD,<sup>64</sup> and  $\text{TiO}_2$  Magnéli phases.<sup>14</sup> Among these electrode materials, Sn electrodes show the highest yield of nitrogen (92%  $\text{N}_2$  and 6%  $\text{N}_2\text{O}$ ) at a cathodic potential of -2.9 V vs Ag/AgCl.<sup>55</sup> During the  $\text{NO}_3^-$  reduction process,  $\text{N}_2$  is the desired end product, but in most situations,  $\text{NH}_3$  is also produced at high yields (e.g., 77.3% on Cu, 75.3% on Zn and 53.3% on Al)<sup>58</sup>. The formation of  $\text{NH}_3$  is undesirable because it is toxic at high concentrations and is a nutrient that can lead to algae growth in receiving waters. Studies on electrodes made of Cu-Ni alloy and BDD show that low yield of  $\text{NH}_3$  can be achieved by polarity reversal during the nitrate reduction process.<sup>14</sup> However, the production of ammonia is still not completely eliminated. In order to eliminate the  $\text{NH}_3$  byproduct, an alternative method using the addition of chloride was proposed.<sup>14</sup> In their study, a combination of cathodic reduction (Ebonex) of nitrate and chloride-mediated

electrochemical oxidation at the Ti/RuO<sub>2</sub> anode was used.<sup>14</sup> The following equations show the oxidation of NH<sub>3</sub> by this pathway:



Several methods for water treatment of NO<sub>3</sub><sup>-</sup> have been briefly summarized in this section, and the existing problems are related to high capital and operation cost and the generation of undesired byproducts. A new technique needs to be developed to improve the treatment of nitrate.

## Chapter III: MATERIALS AND METHODS

### A. Material

Sodium nitrate ( $\text{NaNO}_3$ ), sodium perchlorate ( $\text{NaClO}_4$ ), oxalic acid (OA), potassium ferrocyanide ( $\text{K}_4\text{Fe}(\text{CN})_6$ ), potassium ferricyanide ( $\text{K}_3\text{Fe}(\text{CN})_6$ ), coumarin (COU), 7-hydroxycoumarin (7-HC), terephthalic acid (TA), and 2-hydroxyterephthalic acid (HTA) were obtained from Sigma-Aldrich. All solutions were prepared using Barnstead NANOpure water ( $18.2 \text{ M}\Omega \text{ cm}$ ).

### B. Reactive Electrochemical Membrane Synthesis.

REMs were synthesized from a tubular 50 kDa  $\text{TiO}_2$  ultrafiltration membrane (TAMI Industries; Les Laurons, France). The membrane was cut to 10 cm in length and had inner and outer diameters of 0.5 cm and 1.0 cm, respectively. The  $\text{TiO}_2$  membrane was reduced to a Magnéli phase titanium suboxide ( $\text{Ti}_n\text{O}_{2n-1}$ ) using a high temperature ( $1050^\circ\text{C}$ ) reduction method under 1 atm  $\text{H}_2$  gas in a tube furnace (OTF-1200X, MTI). Reductive treatments were performed for 30 hours to produce a  $\text{Ti}_6\text{O}_{11}$  membrane (REM-1), 40 hours for a mixture of  $\text{Ti}_4\text{O}_7$  and  $\text{Ti}_6\text{O}_{11}$  (REM-2), and 50 hours for a  $\text{Ti}_4\text{O}_7$  membrane (REM-3).

### C. Membrane Characterization.

The membranes were characterized by X-ray diffraction (XRD, Siemens D-5000) with a Cu X-ray tube (40 kV and 25 mA), and scans were collected with DataScan software (MDI, v. 4.3.355, 2005) at a  $0.02^\circ$  degree step size and a 1 s dwell time.<sup>65</sup> Scanning electron

microscopy (SEM, Hitachi S-3000N) was used to characterize the structure of REM at 10 kV from 1 to 3 k magnification. Conductivity measurements were performed using EIS with amplitude of  $\pm 4$  mV and a frequency range of 0.1 to  $3 \times 10^4$  Hz. Conductivity ( $\sigma$ ) was calculated from the membrane cross-sectional area ( $A = 0.589 \text{ cm}^2$ ) and length ( $x = 10 \text{ cm}$ ), using the following equation:

$$\sigma = \frac{x}{R_m A} \quad (3.1)$$

Where  $R_m$  is the measured membrane resistance determined by EIS.

Electroactive surface area of REM-3 was determined by EIS measurements at the OCP ( $\sim 160$  mV), amplitude of  $\pm 4$  mV, and a frequency range of 0.01 to  $3 \times 10^4$  Hz. Experiments were performing in cross-flow filtration mode with a 100 mM  $\text{NaClO}_4$  supporting electrolyte and permeate flux of 803 LMH. A transmission line model (TLM) developed by Jing et al.<sup>66</sup> was used to fit the EIS data.

#### **D. Cross-flow Filtration Setup.**

Filtration experiments were conducted similar to those described by Zaky and Chaplin.<sup>3</sup> The REM was used as working electrode, and a 1.6 mm diameter 316 stainless steel rod was used as counter electrode. A leak-free Ag/AgCl reference electrode (Warner Instruments, LF-100) was placed  $\sim 0.85$  mm from the inner REM surface. Potentials were applied and monitored using a Gamry Reference 600 potentialstat/galvanostat. For EIS measurements, a silver wire was used as a pseudo reference electrode, due to the high impedance of the Ag/AgCl reference. All potentials were corrected for solution resistance, which was calculated by EIS measurements, and potentials are reported versus the standard hydrogen

electrode (SHE). Reynolds numbers for membrane cross-flow ranged between 312 and 1247 (laminar).

### E. Cross Flow Filtration Experiment

**Reaction Rate Characterization.** The intrinsic surface area normalized kinetic rate constant ( $k$ ) for  $\text{Fe}(\text{CN})_6^{4-}$  oxidation was determined by linear sweep voltammetry (LSV) in filtration mode with a 103 kPa trans-membrane pressure ( $\Delta P$ ). The solution contained 5 mM  $\text{Fe}(\text{CN})_6^{4-}$  in a 100 mM  $\text{KH}_2\text{PO}_4$  background electrolyte. Increased scan rate ( $v$ ) during LSV will cause a shift in the oxidation peak current ( $i_p$ ) to higher anodic potentials, and  $k$  can be determined from a plot of  $i_p$  versus peak potential ( $E_p$ ). The following equation is used for an irreversible electron transfer:<sup>67,68</sup>

$$\ln(i_p) = -\alpha f(E_p - E^{0'}) + \ln(0.227FAC_b k) \quad (3.2)$$

Where  $C_b$  is the bulk concentration ( $\text{mol m}^{-3}$ );  $E^{0'}$  is the formal potential;  $\alpha = 0.5$  is the transfer coefficient;  $f = F/RT$ ; and other parameters have their usual meanings. A value for  $E^{0'}$  was determined by measurement of the open circuit potential (OCP) of the solution.

The observed rate constant ( $k_{obs}$  ( $\text{m s}^{-1}$ )) for  $\text{Fe}(\text{CN})_6^{4-}$  oxidation at the REM was determined using the limiting current approach, and  $k_{obs}$  was calculated the following equation.

$$k_{obs} = \frac{I_{lim}}{zFA_i C_b} \quad (3.3)$$

Where  $A_i$  is the internal REM surface area ( $\text{m}^2$ );  $I_{lim}$  is the limiting current (A); and  $z = 1$  is the number of electrons transferred. Experiments were conducted with a solution of 5 mM  $\text{Fe}(\text{CN})_6^{4-}$  and 5 mM  $\text{Fe}(\text{CN})_6^{3-}$  in a 100 mM  $\text{KH}_2\text{PO}_4$  supporting electrolyte, and  $I_{lim}$  was determined by scanning the anodic potential at  $v = 100 \text{ mV s}^{-1}$ , starting at the OCP. The

permeate flux ( $J$ ) was controlled by varying  $\Delta P$  (0 to 103 kPa). An additional measurement of  $I_{lim}$  at REM-3 was performed at a  $v = 10 \text{ mV s}^{-1}$  and in an electrolyte consisting of 5 mM  $\text{Fe(CN)}_6^{4-}$ , 20 mM  $\text{Fe(CN)}_6^{3-}$ , and 100 mM  $\text{KH}_2\text{PO}_4$  in order to insure that neither cathodic reactions nor non-faradaic current interfered with  $I_{lim}$  measurements. The REM was initially operated with a permeate flux of 800 LMH, where both feed and permeate solutions were recycled for 30 min. After which, LSV was performed at  $J = 110$  to 950 LMH, in order to assess the effect of  $J$  on  $k_{obs}$ .

**Oxyanion separation.** Nitrate separation experiments were conducted with 1 and 10 mM  $\text{NaNO}_3$  solutions. Perchlorate separation experiments were performed with a 9 mM  $\text{NaClO}_4$  solution. The REM was polarized as cathode and the stainless rod as anode. Cell potentials from 0 to 10 V were tested. The following equation was derived from the extended Nernst-Planck equation and was used to simulate  $\text{ClO}_4^-$  and  $\text{NO}_3^-$  concentrations in the permeate stream.<sup>15</sup>

$$C_{p,j} = \frac{C_{f,j}u - \frac{z_j F}{RT} D_j C_{f,j} \frac{\Phi}{L}}{J_i} \quad (3.4)$$

where  $J_i$  is the membrane permeate water flux ( $\text{m s}^{-1}$ ) calculated at the inner membrane surface;  $D_j$  is the diffusion coefficient for species  $j$  ( $\text{m}^2 \text{ s}^{-1}$ ) ( $1.32 \times 10^{-9}$  for  $\text{NO}_3^-$  and  $1.7 \times 10^{-9}$  for  $\text{ClO}_4^-$ );<sup>69,70</sup>  $C_{p,j}$  and  $C_{f,j}$  are the ion concentrations of species  $j$  in the permeate and feed solutions, respectively ( $\text{mol m}^{-3}$ );  $\Phi$  is the applied cell potential (V);  $u$  is the average solution velocity in the membrane pore entrance ( $\text{m s}^{-1}$ ); and  $L$  is the distance between the anode and cathode ( $1.7 \times 10^{-3} \text{ m}$ ).

**Reactivity Probes.** There are two active mechanisms for compound oxidation at the REM, direct electron transfer and oxidation by  $\text{OH}^\bullet$ .<sup>71</sup> OA was chosen as a direct oxidation probe, as



its reactivity with OH<sup>•</sup> is low ( $1.4 \times 10^6 \text{ M}^{-1} \text{ s}^{-1}$ ).<sup>72-74</sup> COU and TA were chosen as OH<sup>•</sup> probes, as they have been reported to be resistant to direct oxidation and both readily react with OH<sup>•</sup> to form fluorescent 7-HC<sup>35</sup> and HTA<sup>75</sup> products, respectively. The second-order rate constants for COU and TA with OH<sup>•</sup> are  $6.2 \times 10^9 \text{ M}^{-1} \text{ s}^{-1}$  and  $4.0 \times 10^9 \text{ M}^{-1} \text{ s}^{-1}$ , respectively.<sup>76,77</sup>

Oxidation experiments with feed concentrations of OA (1 mM), COU (1 mM), and TA (0.1 mM) were prepared in a 2-L, electrochemically inert, 100 mM NaClO<sub>4</sub> supporting electrolyte solution.<sup>78,79</sup> Before applying an electrode potential, feed and permeate solutions were recycled for 20-30 min through the REM to reach steady state and to assess compound adsorption. After which, an anodic potential was applied to the REM and the permeate solution was no longer recycled. For OA oxidation an anodic potential of 2.94 V was applied to the REM; for COU oxidation anodic potentials of 2.64 and 3.14 V were applied; and for TA oxidation anodic potentials of 2.14 and 2.64 V were applied.

Current efficiency was calculated by:

$$\text{CE} = \frac{JFz(C_{f,j} - C_{p,j})}{I} * 100 \quad (3.5)$$

where  $J$  is the permeate flux rate on the outer membrane surface;  $z$  is the number of electrons transferred per molecule;  $I$  is the current density. All experiments were performed at room temperature ( $21 \pm 2^\circ\text{C}$ ).

## F. Analytical Method

Concentrations of COU and TA were determined using HPLC with a C18 (2) column (250 x 4.6 mm, Luna) and a photodiode array detector (wavelength = 254 nm) (SPD-M30A, Shimadzu). HPLC with a fluorescent detector (RF-20A, Shimadzu) was used for 7-HC ( $\lambda_{\text{ex}} =$

---

332 nm and  $\lambda_{\text{em}} = 471$  nm) and HTA ( $\lambda_{\text{ex}} = 315$  nm and  $\lambda_{\text{em}} = 435$  nm) quantification.

Concentrations of OA,  $\text{NO}_3^-$ , and  $\text{ClO}_4^-$  were measured using ion chromatography (Dionex ICS-2100; Dionex IonPac AS16 Column). The pH was measured using a multi-function meter and probe (PC2700, Oakton).

## Chapter IV: RESULT AND DISCUSSION

### A. Physical Characterization.

The TiO<sub>2</sub> membrane and Magnéli phase REMs were characterized by X-Ray Diffraction (XRD) (Figure 1). The XRD data for the TiO<sub>2</sub>, REM-1, REM-2, and REM-3 membranes are shown in Figures 1a, 1b, 1c, and 1d, respectively, and the XRD standards for Ti<sub>4</sub>O<sub>7</sub>, Ti<sub>6</sub>O<sub>11</sub>, and TiO<sub>2</sub> are shown in Figures 1e, 1f, and 1g, respectively. Comparing the XRD data for the membranes to the standard data shows that the TiO<sub>2</sub> membrane was comprised of high purity TiO<sub>2</sub>, and more reduced Magnéli phases developed with prolonged reduction times. The XRD data for REM-1 (30 hour H<sub>2</sub> treatment) showed only the characteristic peak for Ti<sub>6</sub>O<sub>11</sub> (22.84°) and peaks for other Magnéli phases were not observed. REM-2 (40 hour H<sub>2</sub> treatment) showed a decrease in the characteristic peak for Ti<sub>6</sub>O<sub>11</sub>, and the emergence of the characteristic peak for Ti<sub>4</sub>O<sub>7</sub> (20.78°) (Figure 1c). REM-3 (50 hour H<sub>2</sub> treatment) showed only the characteristic peak for Ti<sub>4</sub>O<sub>7</sub> (Figure 1d). The conductivity of the REMs increased in accordance with prolonged reduction time, and the conductivity increase agreed with the reported conductivity trend of the detected Magnéli phases.<sup>15</sup> The TiO<sub>2</sub> membrane had a conductivity of  $2.55 \times 10^{-5} \text{ S m}^{-1}$ . The conductivity of REM-1, REM-2, and REM-3 were 56.6, 221, and 1132  $\text{S m}^{-1}$ , respectively.

The SEM image shown in Figure 1h represents the cross-sectional structure of REM-3. The membrane consists of two Magnéli phase ceramic layers, the large pore support layer and small pore active filtration layer. The support layer is about 0.25 cm thick with 1-5  $\mu\text{m}$  pores, and the active layer is  $\sim 70 \mu\text{m}$  thick with  $< 1 \mu\text{m}$  pores. It is anticipated that the small pores of

the active layer will lead to enhanced radial mass transport rates of aqueous compounds to the pore wall and thus increased reactivity compared to our prior work.<sup>2,3</sup> Additionally, the large pores of the support layer will reduce  $\Delta P$  during filtration.

The pore structure of REM-3 and the  $\text{TiO}_2$  membrane were characterized by Hg porosimetry, and results are presented in the Figure 6, Appendix A. Porosimetry results for the  $\text{TiO}_2$  membrane determined a porosity ( $\theta$ ) of 0.327, specific surface area of  $0.820 \text{ m}^2 \text{ g}^{-1}$ , and median pore diameter of  $3.67 \text{ }\mu\text{m}$  (based on pore volume data). Porosimetry results for REM-3 determined  $\theta = 0.304$ , specific surface area of  $0.658 \text{ m}^2 \text{ g}^{-1}$ , and median pore diameter of  $2.99 \text{ }\mu\text{m}$ . These slight changes to the pore structure upon reduction to  $\text{Ti}_4\text{O}_7$  were attributed to sintering of the nanopores ( $< 10 \text{ nm}$ ), which is evident by comparing cumulative surface area versus pore diameter plots for the two membranes shown in the Figure 6, Appendix A. Due to the large volume of the support layer compared to the active layer ( $\sim 52$ -fold higher), characterization of the active layer pore structure by Hg porosimetry was not possible. The sintering process resulted in a 3-fold increase in the permeate flux for REM-3 versus the  $\text{TiO}_2$  membrane (Figure 7, Appendix B), which is likely due to the elimination of the  $\sim 1.0 \text{ }\mu\text{m}$  pores that were observed for  $\text{TiO}_2$  but not for REM-3 (Figure 6, Appendix A).

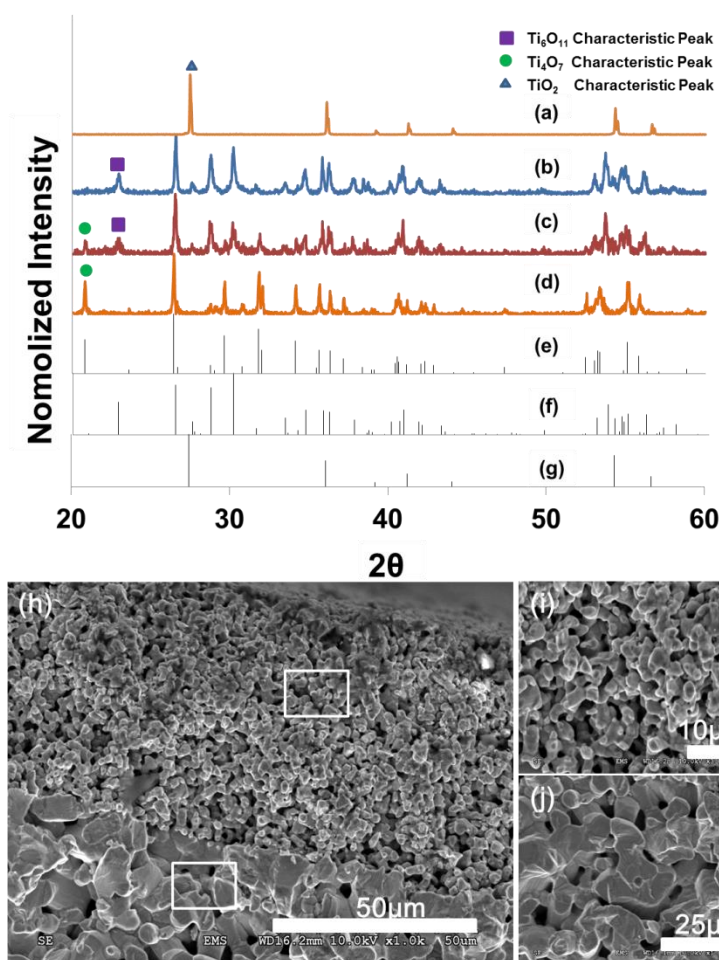


**Figure 1.** XRD data for: (a) Precursor  $\text{TiO}_2$  membrane, (b) REM-1, (c) REM-2, (d) REM-3, (e)  $\text{Ti}_4\text{O}_7$  standard, (f)  $\text{Ti}_6\text{O}_{11}$  standard, and (g)  $\text{TiO}_2$  standard. SEM images: (h) cross-section of REM-3 showing a top active layer and underlying support; (i) active layer (top white box in (h)); and (j) support layer (bottom white box in (h)).

EIS measurements of REM-3 and the TLM model fit of the data are shown in the Figure 8, Appendix C. The total electro-active surface area estimate was  $3.87 \times 10^{-1} \pm 1.79 \times 10^{-2} \text{ m}^2$ , and was distributed as:  $0.8 \pm 0.2\%$  outer surface,  $30.7 \pm 2.2\%$  active layer, and  $68.5 \pm 2.1\%$  support layer. The total specific surface area was  $2.90 \times 10^{-2} \pm 1.34 \times 10^{-3} \text{ m}^2 \text{ g}^{-1}$ , indicating that  $\sim 4.4\%$  of the total surface area was electroactive. This measurement is 3-fold higher than measured previously with a symmetric Ebonex REM.<sup>3</sup> The roughness factor was  $246.3 \pm 11.4$  (based on inner surface area), and is comparable to the studies of porous gold

electrodes.<sup>80</sup> The roughness factor for REM-3 is 2.5-fold less than that previously reported for the symmetric Ebonex REM ( $619 \pm 29$ ).<sup>3</sup> However, the specific surface area of the Ebonex membrane was 4.2-fold higher than measured for REM-3, which is due to a higher nanopore surface area.<sup>3</sup>

## B. Reactivity Characterization.

In order to determine the limiting mechanism for compound oxidation during REM filtration experiments (mass transport versus kinetic limitation), the kinetics of  $\text{Fe}(\text{CN})_6^{4-}$  oxidation ( $k_{obs}$ ) were measured as a function of  $J$  using equation (3.3) (Figure 2a). Previous work<sup>3</sup> indicated that  $k_{obs}$  was limited by convection at low fluxes (up to  $2.8 \times 10^{-5} \text{ m s}^{-1}$ , or  $49.3 \text{ LMH bar}^{-1}$ ), and the measured  $k_{obs}$  was equal to  $J$ . However, the very high  $J$  values (up to  $9.2 \times 10^{-4} \text{ m s}^{-1}$ , or  $3208 \text{ LMH bar}^{-1}$ ) obtained with the REMs developed here were 33-fold (or 65-fold, if normalized by pressure) higher than those previously reported.<sup>3</sup> The flux data shows that the REM developed in this study had a large improvement in permeability at low  $\Delta P$  values, which is a significant improvement compared to our prior work.<sup>3</sup> These very high membrane fluxes were found to be controlled by the porous structure of the support (Figure 9, Appendix D) and resulted in plateauing of the  $k_{obs}$  values (Figure 2a), suggesting a kinetic limitation. The data for  $k_{obs}$  versus  $J$  for all three REMs indicate that the more reduced Magnéli phases had higher  $k_{obs}$  values for  $\text{Fe}(\text{CN})_6^{4-}$  oxidation. The plateau value for  $k_{obs}$  increases in accordance with prolonged synthesis reduction times, with values for REM-1, REM-2 and REM-3 of  $7.76 \times 10^{-5} \text{ m s}^{-1}$ ,  $9.35 \times 10^{-5} \text{ m s}^{-1}$ , and  $1.69 \times 10^{-4} \text{ m s}^{-1}$ , respectively.

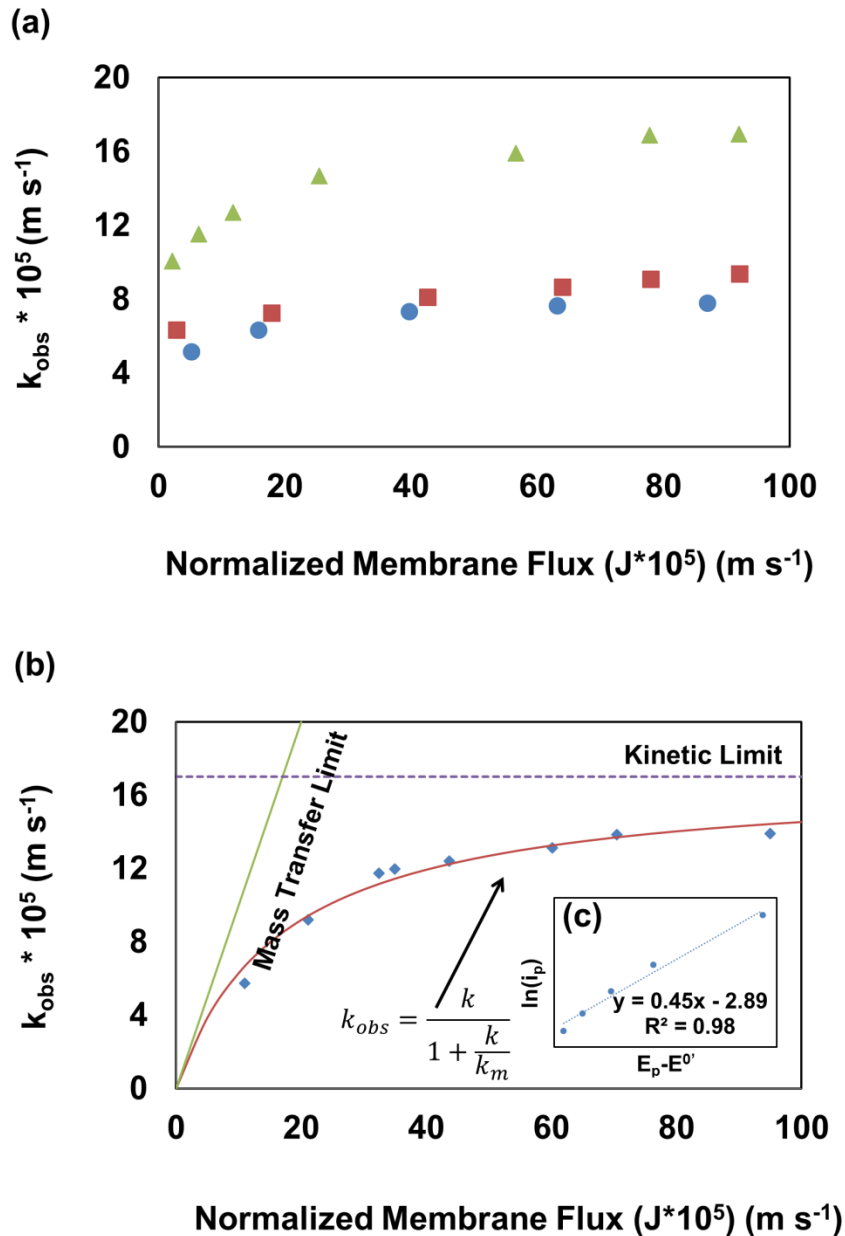


**Figure 2.** Plot of  $k_{obs}$  as a function of  $J$  at  $T = 21 \text{ }^\circ\text{C}$  for a solution of  $5 \text{ mM Fe(CN)}_6^{4-/3-}$  and  $100 \text{ mM KH}_2\text{PO}_4$ . (a) REM-1 (triangles), REM-2 (squares) and REM-3 (circles) at  $\nu = 100 \text{ mV s}^{-1}$ . (b) Measured  $k_{obs}$  for REM-3 at a scan rate of  $10 \text{ mV s}^{-1}$  for a solution of  $5 \text{ mM Fe(CN)}_6^{4-}$ ,  $20 \text{ mM Fe(CN)}_6^{3-}$  and  $100 \text{ mM KH}_2\text{PO}_4$ . Solid red line represent equation (4.1) model fit, and solid green line is convective mass transfer limit calculated by  $k_{obs} = J$ . (c) shows a plot of natural log of peak current versus peak potential. The dash line in (c) represents the linear fit of data points. The interception of the linear equation is used to estimate  $k$  according to equation (3.2). Error bars represent 95% confidence intervals and are contained within data points.

Results in Figure 2a were obtained at  $v = 100 \text{ mV s}^{-1}$ , where the charging current may contribute to the total current and cause an overestimation of  $k_{obs}$ . To measure  $k_{obs}$  more precisely, another experiment with REM-3 was conducted at  $v = 10 \text{ mV s}^{-1}$ . The  $k_{obs}$  value plateaued at around  $1.4 \times 10^{-4} \text{ m s}^{-1}$ , which is 17% lower than that obtained at  $v = 100 \text{ mV s}^{-1}$  (Figure 2b). Figure 2b also includes a model fit (red line) to the measured  $k_{obs}$  values (equation 4.1), which accounts for the competition between kinetics and mass transfer, according to:

$$k_{obs} = \frac{k}{1 + \frac{k}{k_m}} \quad (4.1)$$

where  $k_m$  is the mass transfer rate constant ( $\text{m s}^{-1}$ ). The value for  $k_m$  was set equal to  $J$ , which was deemed appropriate based on prior work that determined mass transfer was convection-limited in REMs where  $k_{obs}$  values were much less than the pore diffusion rate constant.<sup>3</sup> The pore diffusion rate constant ( $k_d$ ) can be estimated as  $k_d = D/r$ , where  $D$  is the diffusion coefficient ( $D = 1 \times 10^{-9} \text{ m}^2 \text{ s}^{-1}$ ) and  $r$  is the median pore radius determined by Hg porosimetry ( $r = 1.49 \text{ }\mu\text{m}$ ). These values provide an estimate of  $k_d = 6.7 \times 10^{-4} \text{ m s}^{-1}$ , which is a conservative estimate given the active layer pore radius is much smaller. Nevertheless, the estimated  $k_d$  value is 4.8-fold higher than the highest measured  $k_{obs}$  value, and indicates that mass transfer was limited by convection and not pore diffusion. Thus the plateauing of the  $k_{obs}$  data at high  $J$  values was related to kinetic limitations. Fitting equation (4.1) to the measured data yielded a value of  $k = 1.7 \times 10^{-4} \text{ m s}^{-1}$ , which is assumed the kinetic limit. An independent estimate of  $k$  was calculated using equation (3.2), and a similar value ( $1.64 \times 10^{-4} \text{ m s}^{-1}$ ) was determined. Our highest value for  $k_{obs}$  ( $1.4 \times 10^{-4} \text{ m s}^{-1}$ ) is the highest reported in the literature for an electrochemical flow-through reactor and 5.4-fold larger than the highest



value reported by Zaky and Chaplin ( $2.6 \times 10^{-5} \text{ m s}^{-1}$ ).<sup>3</sup> Our results are 40% higher than the highest rate constants reported for electrochemical carbon nanotube flow-through reactors ( $1.7 \times 10^{-5}$  to  $1.0 \times 10^{-4} \text{ m s}^{-1}$ ).<sup>81-83</sup> Additionally, the  $k_{obs}$  value reported here was obtained with  $\Delta P = 103 \text{ kPa}$  versus  $206 \text{ kPa}$  used by Zaky and Chaplin.<sup>3</sup> These results indicate that the asymmetric REM-3 had superior mass transfer to the symmetric Ebonex REM, which allowed the kinetic limit of the REM-3 to be realized. Therefore, further improvements of intrinsic kinetic reactivity is needed to reach the upper bound of reaction rates that are made possible by the enhanced mass transport rates of the REM.

### C. Electrochemical Oxidation of Oxalic Acid.

OA is used as a direct oxidation probe.<sup>72</sup> Experiments were conducted on REM-2 and REM-3 to determine the reactivity of OA as a function of the Magnéli phase. Figure 3a shows an example of experimental results with REM-3 for OA oxidation at  $J = 390 \text{ LMH}$ . The first 40 minutes of the experiment was conducted at the OCP, and the similar concentrations in the feed and permeate indicate adsorption was not occurring. After an anodic potential (2.94 V) was applied ( $> 40 \text{ min}$ ), an OA conversion of  $85.3 \pm 4.0\%$  in the permeate stream was achieved. Figure 3b shows a summary of the OA experiments, which includes the calculated OA removal rates as a function of  $J$ . The data clearly shows that the REM-3 was much more reactive than REM-2. The maximum OA removal was  $401.5 \pm 18.1 \text{ mmole h}^{-1} \text{ m}^{-2}$  at  $793 \text{ LMH}$  for REM-3 and  $177.3 \pm 6.02 \text{ mmole h}^{-1} \text{ m}^{-2}$  at  $194 \text{ LMH}$  for REM-2. These  $J$  values were within the same range that  $k_{obs}$  for  $\text{Fe}(\text{CN})_6^{4-}$  oxidation was observed to plateau in Figures 2a and 2b. After the maximum OA reaction was reached, the rates decreased due to

lower residence times in the REM, which suggest that the kinetic limit for OA was achieved. Figure 3c shows the CE calculated by equation (3.5). The highest CE for REM-3 was between  $84.1 \pm 2.7\%$  and  $83.4 \pm 0.9\%$  at  $J = 561\text{-}793$  LMH and for REM-2 was  $48.9 \pm 0.9\%$  at  $J = 194$  LMH. The increase of CE at low fluxes was due to an increase in the convective mass transfer rate. Once OA removal was kinetically limited, the drop of CE at higher fluxes was due to competition from the oxygen evolution reaction. Figure 10, Appendix E, shows polarization curves for oxygen evolution as a function of  $J$ . Higher  $J$  values increased the current for oxygen evolution by sweeping gas bubbles from the REM surface. In previous work by Zaky and Chaplin,<sup>3</sup> the removal rate in the permeate was  $390 \pm 26$  mmole  $\text{h}^{-1} \text{m}^{-2}$  at 2.9 V and  $74 \pm 10$  LMH, and the current efficiency was only  $59.3 \pm 3.9\%$ . Once again, the superior flux properties of the REM-3 compared to the symmetric Ebonex REM used in our prior work results in this higher CE. Additionally, it was shown that  $\text{Ti}_4\text{O}_7$  (REM-3) is more active for OA oxidation than the less reduced  $\text{Ti}_6\text{O}_{11}$  Magnéli phase (REM-2).

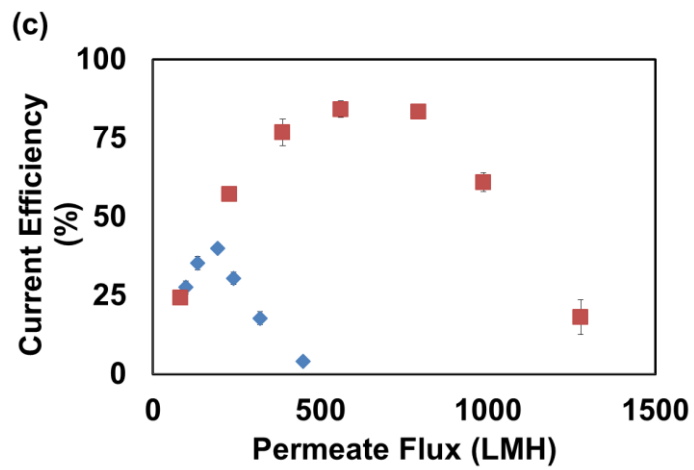
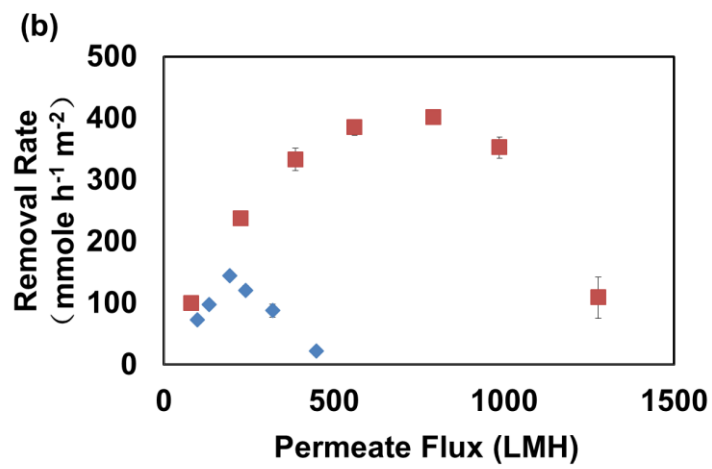
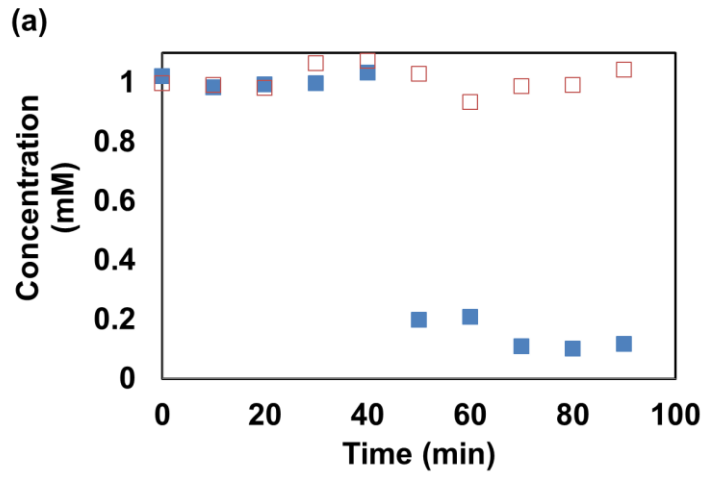


**Figure 3.** (a) Concentration profile of feed and permeate during oxalic acid oxidation on REM-3 at  $J = 390$  LMH. (b) Calculated removal rate of OA as a function of  $J$ . (c) Current efficiency of data in (b). REM-3 (red squares) and REM-2 (blue diamonds). Experimental conditions:  $T = 21$  °C; Potential = 2.94 V; Electrolyte = 100 mM NaClO<sub>4</sub>. Error bars represent 95% confidence intervals ( $n = 4$ ).

#### D. Hydroxyl Radical Probe Studies.

To assess the production of OH<sup>•</sup> on the REM, COU and TA were used as OH<sup>•</sup> probes. Separate control experiments were performed in a divided cell reactor, which confirmed COU and TA removal was due to anodic reactions (data not shown). Oxidation experiments with COU were conducted at the OCP, 2.64, and 3.14 V ( $J = 98$  LMH), and the formation of 7-HC was used as a qualitative OH<sup>•</sup> probe. Results are summarized in Figure 4 and duplicate experiments are provided in the Figure 11, Appendix F. Removal of COU was only achieved at REM-3 ( $62.4 \pm 1.3\%$ ), and at an anodic potential of 3.14 V (Figure 4a). COU removal was neither observed at the OCP nor at 2.64 V (data not shown). The formation of 7-HC was between 0.14 and 0.27  $\mu$ M during the 3.14 V oxidation experiment (Figure 4b), which indicates the existence of OH<sup>•</sup> during the oxidation process. The low 7-HC yield is due to attack of OH<sup>•</sup> at other positions of COU and the degradation of 7-HC to other products.<sup>84</sup> The oxidation of COU and the generation of 7-HC on REM-3 and not REM-2 indicate that a high percentage of Ti<sub>4</sub>O<sub>7</sub> in the anode is necessary for the OH<sup>•</sup> production, and that Ti<sub>6</sub>O<sub>11</sub> is not active for OH<sup>•</sup> production.

TA was chosen as a second OH<sup>•</sup> probe, as there are reports that COU is reactive on carbon electrodes, which are not known to form OH<sup>•</sup>.<sup>85</sup> The experiments were performed with REM-3 at the OCP and anodic potentials of 2.14 and 2.64 V ( $J = 116$  LMH). Removal of TA was not observed at the OCP (0-20 min), was removed  $18.7 \pm 2.0\%$  in the permeate stream at

an anodic potential of 2.14 V (20-40 min), and was removed  $57.8 \pm 1.2\%$  at an anodic potential of 2.64 V ( $> 40$  min) (Figure 4c). Figure 4d shows the detection of HTA in the permeate stream, which indicates that HTA concentrations approximately doubled upon raising the potential from 2.14 to 2.64 V. The yield of HTA was  $0.03 \pm 0.03\%$  at 2.14 V and  $0.1 \pm 0.06\%$  at 2.64 V. Reported  $\text{OH}^\bullet$  generation potentials are above 2.2 V, and at potentials higher than 2.8 V significant concentrations of  $\text{OH}^\bullet$  form.<sup>86-89</sup> Therefore, our experimental results are consistent with the standard electrode potential for the  $\text{OH}^\bullet$  generation half reaction ( $\text{H}_2\text{O} \leftrightarrow \text{OH}^\bullet + \text{H}^+ + \text{e}^-$ ) ( $E^\circ = 2.38$  V),<sup>90</sup> and provide conclusive evidence for  $\text{OH}^\bullet$  formation on the  $\text{Ti}_4\text{O}_7$  anode (REM-3).

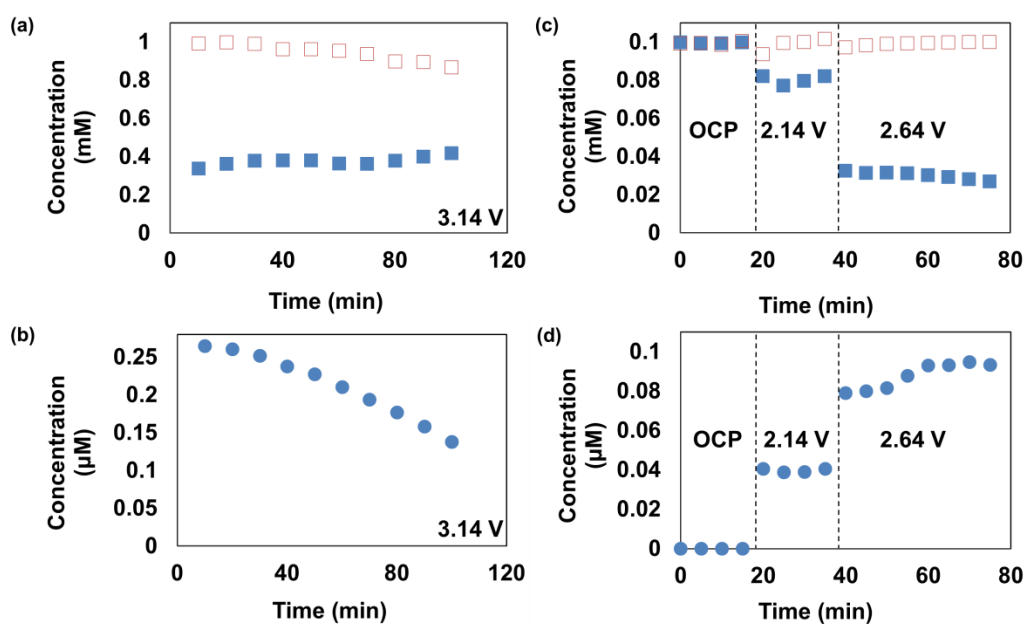


**Figure 4.** (a) Concentration profile of COU in the feed and permeate solutions of REM-3 ( $J = 98$  LMH). Anodic potential is 3.14V. (b) The generation of 7-HC during COU oxidation. (c) Concentration profile of TA in the feed and permeate solutions of REM-3. Anodic potential: OCP (0-20 min); 2.14 V (20-40 min); 2.64 V ( $> 40$  min);  $J = 116$  LMH. (d) Concentration of HTA during TA oxidation. All experiments were conducted in 100mM  $\text{NaClO}_4$  solution and  $T = 21$  °C. Duplicate experiments are shown in Figure 11, Appendix F.

## E. Electrochemical Separation of Oxyanions.

Experiments were also conducted to assess the ability of the REM-3 to reject both  $\text{ClO}_4^-$  and  $\text{NO}_3^-$  via electrostatic separation. For this experiment the REM was polarized as cathode and the stainless steel rod as anode. Feed concentrations of 9 mM  $\text{ClO}_4^-$  and 10 mM  $\text{NO}_3^-$  were tested. Figures 5a and 5b show the permeate concentrations of  $\text{ClO}_4^-$  and  $\text{NO}_3^-$ , respectively, as a function of the cell voltage. TABLE I contains a summary of the experimental parameters and measurements. Cell potentials from 0 to 10 V in 2 V intervals were applied to the REM cell, which corresponded to electric fields up to  $58.6 \text{ V cm}^{-1}$ . When the applied cell potential increased, the concentration of  $\text{ClO}_4^-$  or  $\text{NO}_3^-$  in the permeate solution decreased. The predicted permeate concentrations of  $\text{ClO}_4^-$  and  $\text{NO}_3^-$  are represented in Figure 5 by the dashed lines, which were calculated by the extended Nernst-Planck equation (equation 3.4). The predicted permeate  $\text{ClO}_4^-$  and  $\text{NO}_3^-$  concentrations adequately match measured data, and indicate that oxyanion removal was due primarily to electrostatic repulsion. Evidence for electrochemical reduction was not found, as neither  $\text{NH}_4^+$  nor reduced  $\text{ClO}_x^-$  species were detected in solution.

TABLE I summarizes the data from the oxyanion filtration experiments, including an estimate of the energy consumption due to the applied cell potential. For  $\text{NO}_3^-$  filtration experiments, removal ranged from  $14.68 \pm 1.97\%$  at 2 V cell potential to  $68.02 \pm 0.60\%$  at 10

V cell potential, and for  $\text{ClO}_4^-$  filtration experiments removal ranged from  $14.69 \pm 2.60\%$  at 2 V cell potential to  $95.10 \pm 1.08\%$  at 10 V cell potential. The higher  $\text{ClO}_4^-$  removal compared to  $\text{NO}_3^-$  was attributed to a lower permeate flux, 109 LMH versus 170 LMH for  $\text{ClO}_4^-$  and  $\text{NO}_3^-$  experiments, respectively. The energy consumption increased with the cell potential, and was between 0.03 to 13.05  $\text{kWh m}^{-3}$  (0.021 to 1.92  $\text{kWh mol}^{-1}$ ) for  $\text{NO}_3^-$  and between 0.04 to 19.12  $\text{kWh m}^{-3}$  (0.03 to 2.23  $\text{kWh mol}^{-1}$ ) for  $\text{ClO}_4^-$ .

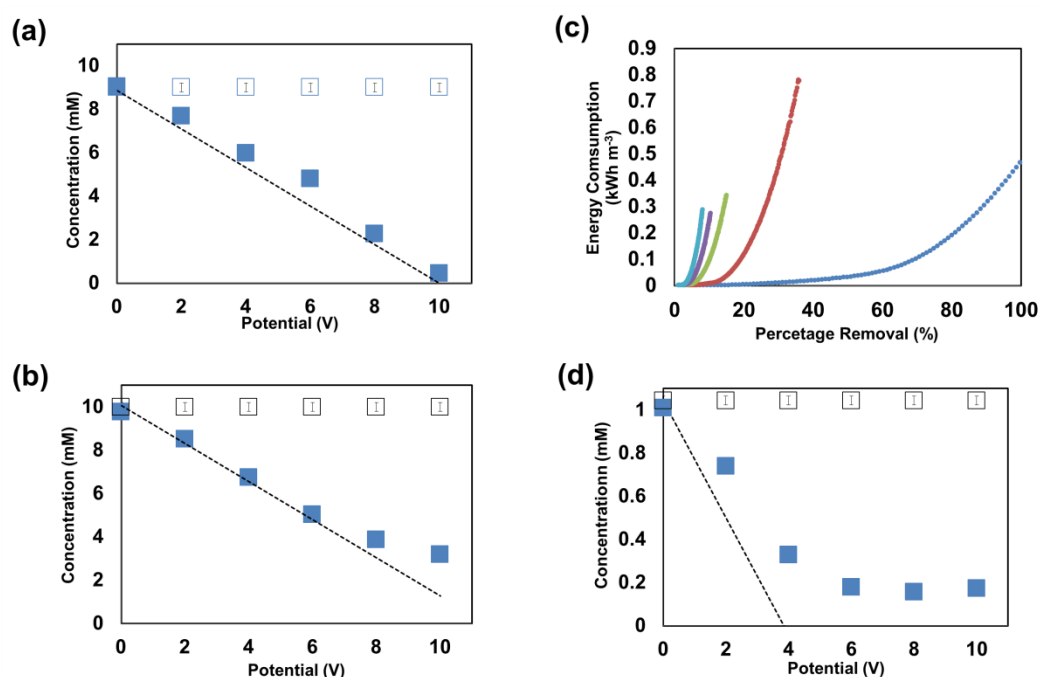


**Figure 5.** Concentration profiles of feed (hollow squares) and permeate (filled squares) during electro-separation of (a) 9 mM  $\text{ClO}_4^-$  ( $J \sim 109$  LMH); (b) 10 mM  $\text{NO}_3^-$  ( $J \sim 170$  LMH); and (d) 1.0 mM  $\text{NO}_3^-$  ( $J \sim 58$  LMH) using REM-3. The feed and permeate solutions were 100% recycled. Cell potentials between 0 and 10 V were applied. Dash lines show the predicted concentration profile using the extended Nernst-Plank equation (equation 3.4). (c) Calculated energy consumption of electro-separation of 1 mM  $\text{NO}_3^-$  under different flow rates (from right to left were  $J = 58, 290, 696, 1006$ , and 1296 LMH). Details of energy consumption are shown in the Figure 12, Appendix G. Error bars represent 95% confidence intervals ( $n = 3$ ) and are contained within data points.  $T = 21$  °C.

**TABLE I**

Summary of data for (A) nitrate (10mM), (B) perchlorate (9 mM), and (C) nitrate (1mM) separation experiments at 21 °C.

<b>A</b>							
Cell Potential (V)	Cathodic Potential (V)	Anodic Potential (V)	Current (A)	pH	Energy (kWh m-3)	Removal (%)	Predicted Removal (%)
0	0	0.00	0	5.33	0	0.0	0.0
2	-0.5	1.40	0.008	5.15	0.03	14.68 ± 1.97	12.3
4	-1.76	2.22	0.108	4.75	0.81	32.38 ± 1.93	24.0
6	-2.98	2.92	0.264	4.53	2.80	49.61 ± 0.74	34.1
8	-4.1	3.77	0.451	4.02	7.13	61.24 ± 1.29	50.8
10	-5.2	4.61	0.681	3.73	13.05	68.02 ± 0.60	61.5
<b>B</b>							
Cell Potential (V)	Cathodic Potential (V)	Anodic Potential (V)	Current (A)	pH	Energy (kWh m-3)	Removal (%)	Predicted Removal (%)
0	0	0.00	0	5.73	0.00	0.0	0.0
2	-0.46	1.50	0.006	5.52	0.04	14.69 ± 2.60	19.3
4	-1.36	2.50	0.078	5.07	0.93	33.72 ± 2.46	38.6
6	-1.9	3.90	0.234	4.65	4.18	46.66 ± 0.72	57.9
8	-2.4	5.30	0.423	4.13	10.08	74.83 ± 2.57	77.2
10	-4.2	5.80	0.642	3.88	19.12	95.10 ± 1.08	96.5
<b>C</b>							
Cell Potential (V)	Cathodic Potential (V)	Anodic Potential (V)	Current (A)	pH	Energy (kWh m-3)	Removal (%)	Predicted Removal (%)
0	0	0.00	0	5.82	0.00	0.0	0.0
2	-0.55	1.31	0.001	5.15	0.01	26.73 ± 1.53	36.3
4	-1.78	2.08	0.01	4.73	0.22	67.33 ± 1.93	72.6
6	-2.77	3.09	0.03	4.41	0.87	82.18 ± 1.76	100.0
8	-4.05	3.81	0.052	4.28	2.01	84.46 ± 0.55	100.0
10	-5.5	4.36	0.085	4.10	4.08	82.67 ± 1.17	100.0



These results provide proof-of-concept that the REM can be used for electrostatic ion separation, but the energy requirements were not optimized. In order to determine more optimal conditions for  $\text{NO}_3^-$  removal, polarization curves (Figure 12, Appendix G) were performed with 1 mM  $\text{NaNO}_3$  solutions,  $J$  values between 58 and 1291 LMH, and cell potentials between 2 and 10 V. Data from polarization curves were used in combination with equation (3.4) to determine energy consumption as a function of  $\text{NO}_3^-$  removal at different  $J$  values (Figure 5c). Calculations show that energy consumption increases drastically with increasing values of  $J$ , due to the high cell potential needed to counter-balance the convective flux. A value of  $J = 58$  LMH was chosen for further experimental study using a 1 mM  $\text{NaNO}_3$  feed concentration, and permeate concentrations for  $\text{NO}_3^-$  are shown in Figure 5d. The decrease of the feed  $\text{NO}_3^-$  concentration from 10 mM to 1 mM caused the conductivity of the electrolyte solution to drop by an order of magnitude, and therefore resulted in much lower current to flow at the same applied cell potential (TABLE I). At a 4 V cell potential  $67.33 \pm 1.93\%$  of  $\text{NO}_3^-$  was removed and energy consumption was  $0.22 \text{ kWh m}^{-3}$  ( $0.33 \text{ kWh mol}^{-1}$ ), and at a 6 V cell potential  $82.18 \pm 0.55\%$  of  $\text{NO}_3^-$  was removed and energy consumption was  $0.87 \text{ kWh m}^{-3}$  ( $1.06 \text{ kWh mol}^{-1}$ ). Permeate concentrations did not reach zero at 8 V and 10 V cell potentials, as predicted by equation (3.4). This observation is attributed to faradaic water reduction reactions on the cathode at the relatively high cathodic potentials of -4.05 V and -5.50 V for 8 V and 10 V cell potentials, respectively. The pH of the recycled feed decreased in all experiments due to the generation of  $\text{H}^+$  on the anode to balance  $\text{NO}_3^-$  rejection and as a parasitic side reaction at high cell potentials.

Electro dialysis (ED) is an effective and mature method for  $\text{NO}_3^-$  removal.<sup>91</sup> Reported energy consumption for ED ranges from 0.044 to 0.107 kWh m<sup>-3</sup> for the removal of 60 to 70% of a 1.27 mM  $\text{NO}_3^-$  feed concentration, respectively.<sup>18</sup> Our experimental results showed an approximate 2-fold higher energy cost compared to ED at a similar  $\text{NO}_3^-$  feed concentration and percent removal. Although ED is still more energy efficient than the REM-3 used for  $\text{NO}_3^-$  separation, conditions were not optimized in our system. A significant reduction in energy consumption can be obtained by optimizing the electrode spacing, fluid dynamics, and anode material, indicating that cost competitive ion separation should be obtainable with the REM.

There are several additional advantages of using the REM over ED related to mineral scaling, organic compound fouling, and chemical robustness. Mineral scaling is a concern for the ED process, as inorganics such as  $\text{Ca}(\text{OH})_2$  and  $\text{CaCO}_3$  can form on the membrane and adversely affect membrane performance.<sup>92</sup> Organic compound fouling is also problematic during ED, as they adsorb on the ion exchange membranes used in ED and cause a significant decrease in process performance, and membrane fouling is sometimes irreversible.<sup>93-95</sup> Both scaling and irreversible organic compound fouling of ion exchange membranes used in ED can be regenerated with strong acid and base treatments, respectively, but significantly reduce the life of the polymeric membranes.<sup>18</sup> However, the REM is made of a chemically resistant Magnéli phase material, and fouling and scaling can be eliminated by either reverse polarity treatment or chemical treatment (acid and base) without adverse effects to the membrane.<sup>15</sup> Further research is necessary to determine the feasibility of using the REM for ion separation,

but initial results are encouraging.

## Chapter V: CONCLUSIONS

This study has developed and characterized a novel  $\text{TiO}_2$  Magnéli phase ultrafiltration membrane. The precursor  $\text{TiO}_2$  membrane was converted to a high purity  $\text{Ti}_4\text{O}_7$  REM in a reductive atmosphere. The membrane has a dual layer structure which was confirmed by SEM, EIS and Hg Porosimetry. This asymmetric structure increased pressure-normalized permeate fluxes. The observed reaction rate was 5.4-fold larger than the maximum value reported by Zaky and Chaplin,<sup>3</sup> and this observed reactivity is the highest reported for an electrochemical flow-through reactor. A comparison of the intrinsic reaction rate constants for different Magnéli phase  $\text{Ti}_n\text{O}_{2n-1}$  ( $n = 4$  to  $6$ ) electrodes indicated  $\text{Ti}_4\text{O}_7$  had the highest reactivity. The novel  $\text{Ti}_4\text{O}_7$  ultrafiltration membrane was tested for the oxidation of organics via the direct electron transfer mechanism (oxalic acid) and formation of  $\text{OH}^\bullet$  (coumarin, and terephthalic acid), and showed larger reactivity and higher permeability than the previous work performed by Zaky and Chaplin.<sup>3</sup>

The sintered  $\text{Ti}_4\text{O}_7$  REM was also tested for oxyanion separation using electrostatic repulsion. The rejection of  $\text{ClO}_4^-$  and  $\text{NO}_3^-$  ions were predicted by the extended Nernst-Planck equation. The energy consumption decreased with lower ionic strength. Compared with electro dialysis (ED), our work showed about a 2-fold higher energy cost for the removal of 60 to 70% of a similar initial concentration of  $\text{NO}_3^-$ . However, several advantages of REM over ED were provided on aspects of mineral scaling and organic compound fouling, and chemical robustness.

So far, there are still several issues that need further investigation. All the experiments conducted for oxyanions separation used DI water as the background solution, without the addition of non-target ions. Thus, the influences of these ions on oxyanion separation still needs to be investigated. Besides, the pore structure is another factor that may affect the oxyanion rejection, and further study using simulation is necessary. The removal of  $\text{NO}_3^-$  in this study was achieved only by electrostatic separation. Some studies have shown that  $\text{NO}_3^-$  can be reduced by electrodes coated with metal catalysts (e.g., Cu, Pd, Ag).<sup>96-99</sup> As the  $\text{Ti}_4\text{O}_7$  Magnéli phase membrane is stable under polarization condition, reactive towards inorganic and organic contaminations, and highly resistive to corrosion, it will be a promising substrate material for coating catalyst to reduce  $\text{NO}_3^-$ . Although the oxidative reactivity reported in this work is the highest in the literature, further improvement of reactivity by doping with other elements (e.g., Nb) would further the impact of REMs in water treatment.

## APPENDICES

## A. Hg Porosimetry

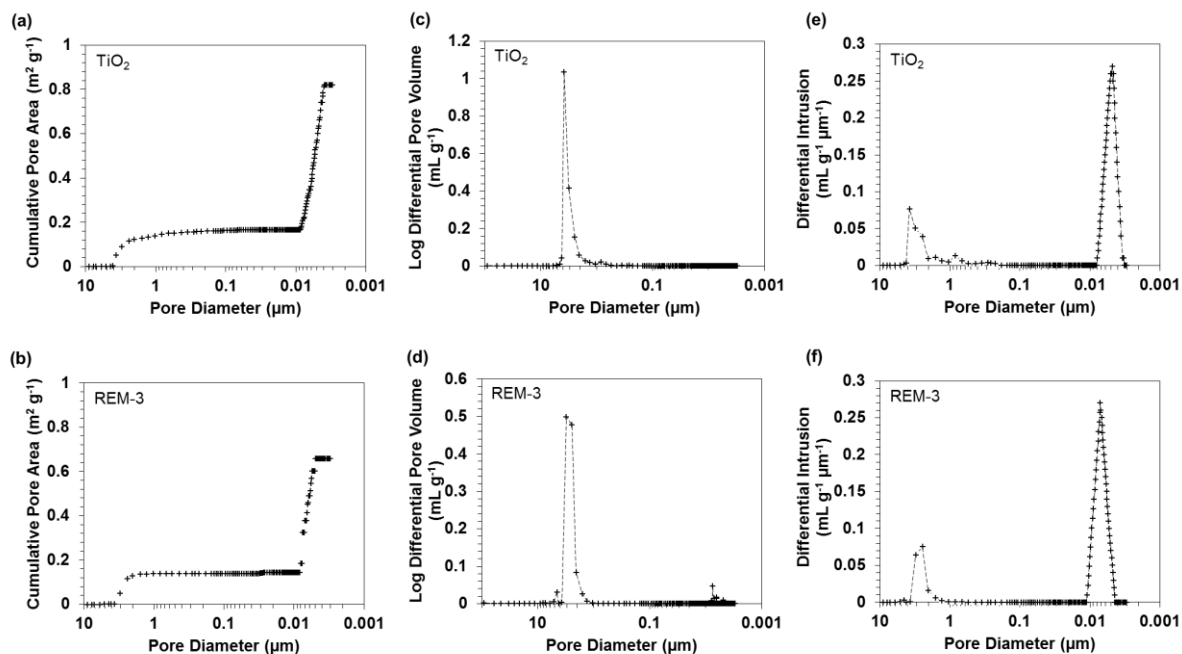


**Figure 6.** Hg porosimetry analysis of cumulative pore area for (a) precursor  $\text{TiO}_2$  membrane (b) REM-3, log differential pore volume data for (c) precursor  $\text{TiO}_2$  membrane and (d) REM-3, and differential intrusion for (e) precursor  $\text{TiO}_2$  and (f) REM-3.

## B. Permeate Flux

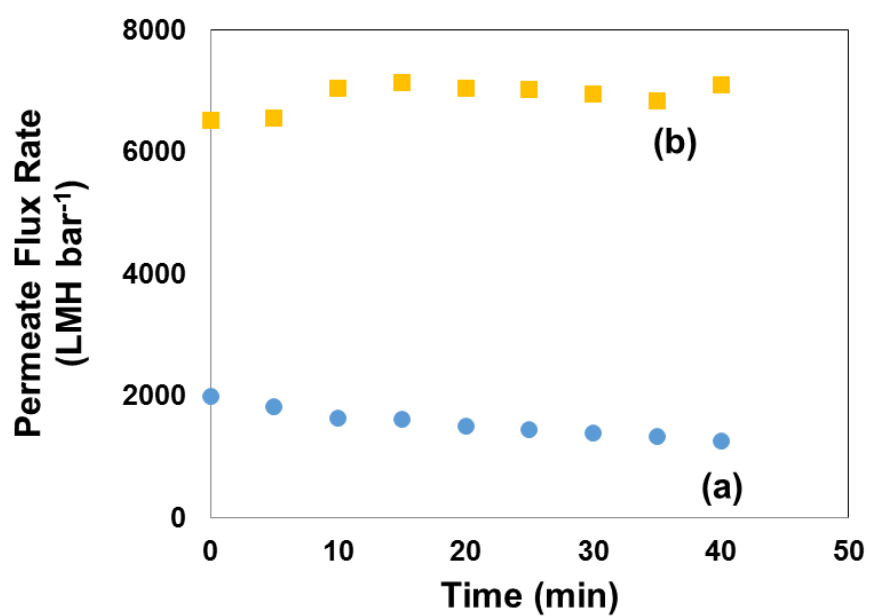


**Figure 7.** Pressure-normalized permeate membrane flux profiles for DI water at 21 °C: (a) TiO<sub>2</sub> membrane, and (b) REM-3. Flux rate was tested at  $\Delta P = 68.9$  kPa and 50 L h<sup>-1</sup> cross flow rate.

### C. EIS Measurement of Electroactive Surface Area

Electroactive surface area of REM-3 was determined by EIS measurements at the OCP (~160 mV), amplitude of  $\pm 4$  mV, and a frequency range of 0.01 to  $3 \times 10^4$  Hz. Experiments were performing in cross-flow filtration mode with a 100 mM NaClO<sub>4</sub> supporting electrolyte and permeate flux of 803 LMH. A transmission line model (TLM) developed by Jing et al.<sup>66</sup> was used to fit the EIS data. The TLM is able to decouple the impedances at  $i$  distinct membrane locations ( $i$  = outer membrane surface, active layer pores, or support layer pores) at the membrane-electrolyte interface. EIS data is used to characterize the electro-active surface area at each location, through calculation of the double layer capacitance ( $C_{dl}$ ) using equation A-1.<sup>100</sup>

$$C_{dl,i} = \left( \frac{Y_{0,i}}{[r_s^{-1} + R_{ct,i}^{-1}]^{1-\alpha}} \right)^{\frac{1}{\beta}} \quad (\text{A-1})$$

Where  $r_s$  is the solution resistance (ohm),  $R_{ct,i}$  is the charge transfer resistance (ohm) of location  $i$ ;  $Y_{0,i}$  is the capacitance (F), and  $\beta$  (dimensionless) is related to an exponential factor that represents the angle of rotation of a purely capacitive line on the complex plane plots. A value of  $60 \mu\text{F cm}^{-2}$  was taken as an estimate of the  $C_{dl}$  for a metal oxide,<sup>101</sup> and was used to calculate the electro-active surface area of REM-3. EIS measurements and TLM fit are shown in Figure S-3.



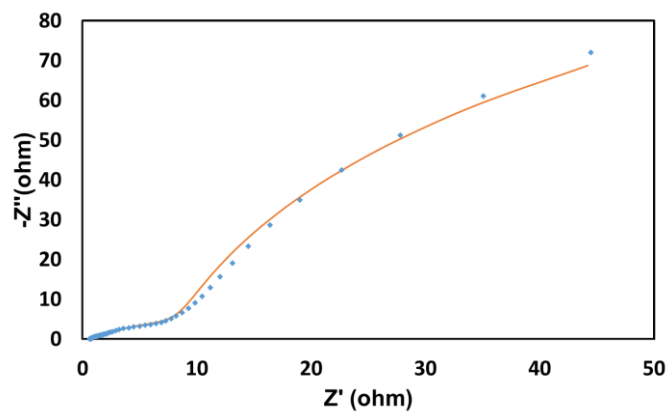


**Figure 8.** Measured EIS data for a solution of 5mM  $\text{Fe(CN)}_6^{4-}$  and 5mM  $\text{Fe(CN)}_6^{3-}$  in 100mM  $\text{NaClO}_4$  electrolyte collected at the OCP and  $T = 21^\circ\text{C}$ . Solid line is the TLM fit.

## D. Oxyanion Separation

Nitrate separation experiments were conducted with 1 and 10 mM  $\text{NaNO}_3$  solutions. Perchlorate separation experiments were performed with a 9 mM  $\text{NaClO}_4$  solution. The REM was polarized as cathode and the stainless rod as anode. Cell potentials from 0 to 10 V were tested. The extended Nernst-Planck equation was used to simulate  $\text{ClO}_4^-$  and  $\text{NO}_3^-$  concentrations in the permeate stream (Equation A-2).<sup>102</sup>

$$N_j = J_i C_{p,j} = -D_j \frac{\partial C_{f,j}}{\partial x} - \frac{z_j F}{RT} D_j C_{f,j} \frac{\partial \Phi}{\partial x} + C_{f,j} u \quad (\text{A-2})$$

Where  $N_j$  is the molar flux of species  $j$  ( $\text{mol m}^{-2} \text{s}^{-1}$ );  $J_i$  is the membrane permeate water flux ( $\text{m s}^{-1}$ ) calculated at the inner membrane surface;  $D_j$  is the diffusion coefficient ( $\text{m}^2 \text{s}^{-1}$ ) ( $1.32 \times 10^{-9}$  for  $\text{NO}_3^-$  and  $1.7 \times 10^{-9}$  for  $\text{ClO}_4^-$ );<sup>69,70</sup>  $C_{p,j}$  and  $C_{f,j}$  are the ion concentrations in the permeate and feed solutions, respectively ( $\text{mol m}^{-3}$ );  $\Phi$  is the applied cell potential (V);  $u$  is the average solution velocity in the membrane pore entrance ( $\text{m s}^{-1}$ );  $R$  is the ideal gas constant ( $\text{J mol}^{-1} \text{K}^{-1}$ ); and  $T$  is the temperature (294 K). The porosity of the REM was  $\theta = 0.304$  (determined by Hg porosimetry analysis), which was applied to estimate  $u$  using equation A-3.

$$u = \frac{J}{\theta} \quad (\text{A-3})$$

The flow conditions in the REM reactor allowed diffusion to be ignored ( $\text{Pe} = 9.85 \times 10^5$ ), and the electric field is assumed to be linear between the anode and cathode, due to the concentric placement of the electrodes. Therefore, equation A-2 is simplified to the following:

$$C_{p,j} = \frac{C_{f,j} u - \frac{z_j F}{RT} D_j C_{f,j} \frac{\Phi}{L}}{J_i} \quad (\text{A-4})$$

where  $L$  is the distance between the anode and cathode ( $1.7 \times 10^{-3}$  m).

A plot of  $u$  versus trans-membrane pressure ( $\Delta P$ ) for REM-3 shows the expected linear trend (Figure 9, Appendix D). An independent estimate of  $u$  using the Hagen-Poiseuille equation was determined using equation (A-5).

$$u = \frac{r_p^2 \Delta P}{8\eta \Delta x} \quad (\text{A-5})$$

where  $r_p$  is the pore radius;  $\eta$  is the fluid viscosity ( $9.78 \times 10^{-4}$  Pa s (21 °C)); and  $\Delta x$  is the membrane thickness that  $\Delta P$  is calculated over. Equation A-5 is used to determine if the  $\Delta P$  across the membrane is due to the hydraulic resistance of the support layer. For this calculation  $\Delta x = 0.5$  cm (entire membrane thickness) and  $r_p$  was used to fit equation A-5 to the  $u$  measurements (Figure 9, Appendix D). A fitted value of  $r_p = 1.52$   $\mu\text{m}$  was determined, which was nearly identical to the median pore radius of 1.49  $\mu\text{m}$  determined by Hg porosimetry measurements (see manuscript and Appendix A). These results indicate that the  $\Delta P$  across the membrane is due to the hydraulic resistance of the support layer, and that the effective pore size of the membrane can be determined from fitting  $r_p$  to measured flux data.

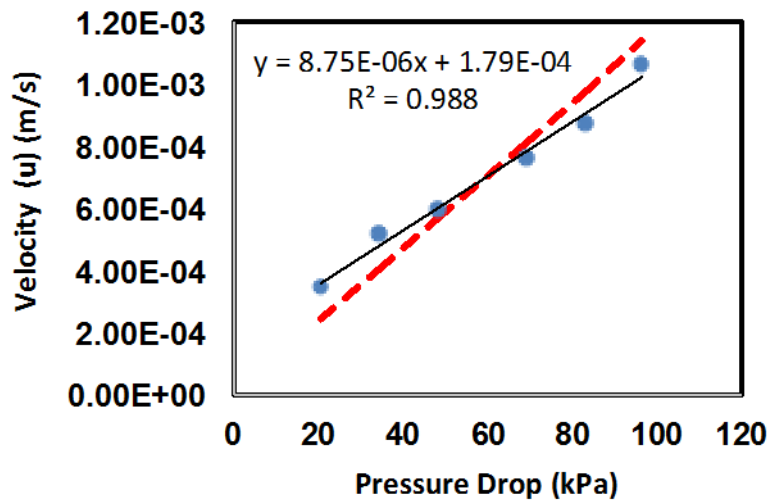


**Figure 9.** Comparison of experimental measurements of  $u$  versus the pressure drop across the membrane (symbols) to equation A-5 (dashed red line). Solid black line represents linear regression of the experimental data.  $T = 21\text{ }^{\circ}\text{C}$ .

### E. Energy Consumption Estimation (Electrolyte)

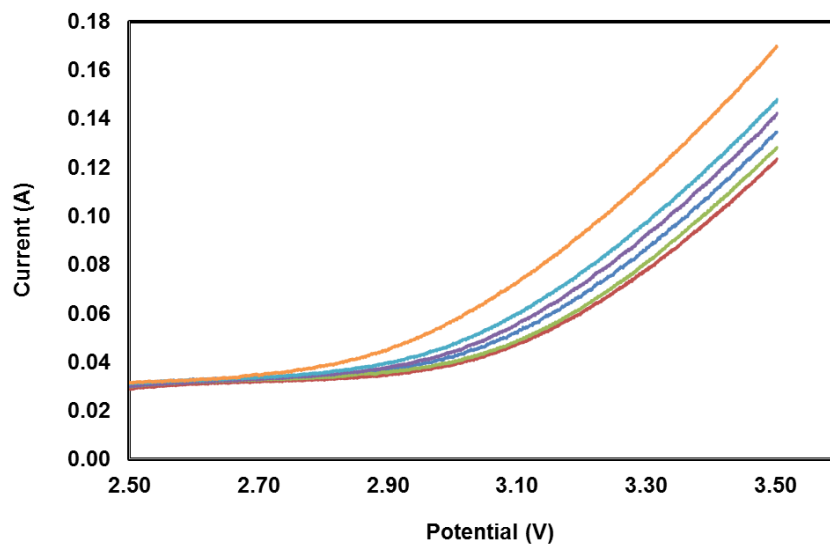


**Figure 10.** Polarization curves with 100mM  $\text{NaClO}_4$  and at  $T = 21^\circ\text{C}$ . From bottom to top, the curves represent polarization profiles for  $J = 62, 193, 400, 561, 968$ , and  $1243$  LMH.

## F. Hydroxyl Radical Probe (Duplicates Experiments)

The following figures show duplicate experiments to those presented in Figure 4 in main text.

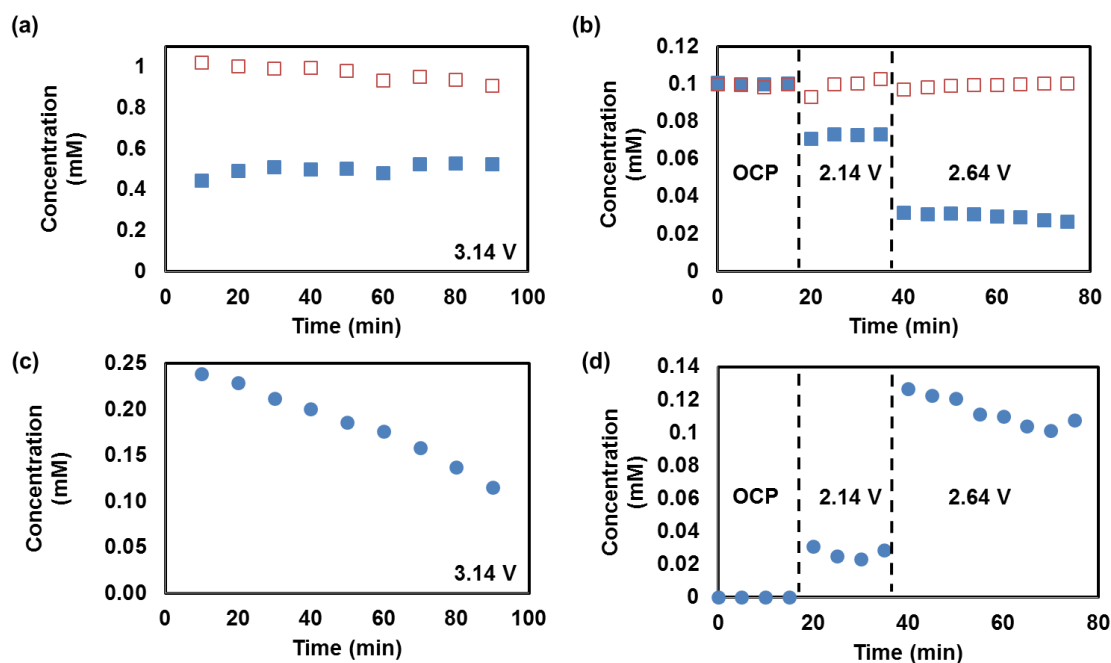


**Figure 11.** (a) Concentration profile of COU in the feed and permeate solutions of REM-3 filtration experiment at  $J = 132$  LMH. Anodic potential is 3.14V/SHE. (b) The generation of 7-HC during COU oxidation. (c) Concentration profile of TA in the feed and permeate solutions of REM-3. Anodic potential: OCP (0-20 min); 2.14 V (20-40 min); 2.64 V (> 40 min).  $J = 110$  LMH. (d) Concentration of HTA during TA oxidation. All experiments were conducted in 100mM NaClO<sub>4</sub> solution and  $T = 21$  °C.

### G. Energy Consumption Estimations (NaNO<sub>3</sub>)

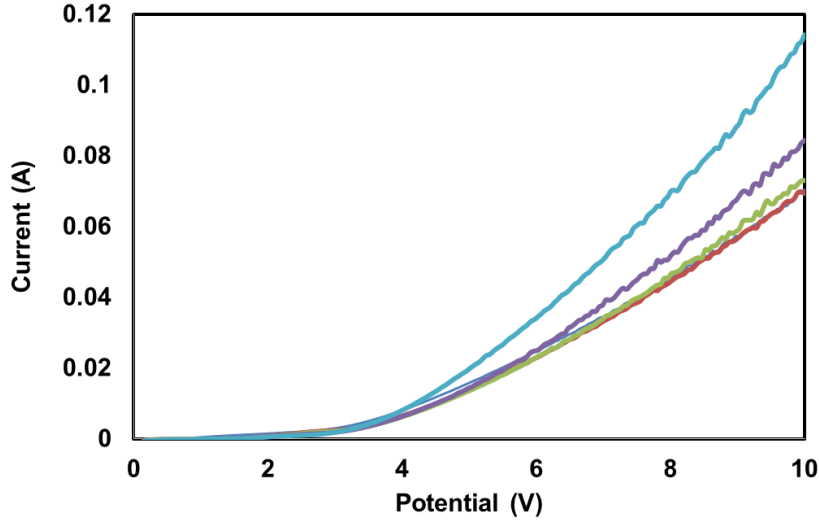


**Figure 12.** Polarization curves with 1mM NaNO<sub>3</sub> at 21 °C. From bottom to top, the curves represent polarization profiles for  $J = 58, 290, 696, 1006,$  and  $1296$  LMH. (Curve for  $J = 58$  and  $290$  LMH overlap.)

The energy consumption was calculated based on measured potential and current at a range of  $J$  values, and the removal percentage was estimated with the corresponding permeate flux value using Nernst-Plank equation (equation 5). A solution containing 1mM NO<sub>3</sub><sup>-</sup> was prepared in 2L DI water without the addition of a supporting electrolyte. Permeate fluxes of  $J = 58, 290, 696, 1006$  and  $1296$  LMH were tested. Under each  $J$  value, a linear sweep voltammetry scan was performed from 0 to 10 V. Energy consumption (EC) in kWh m<sup>-3</sup> was calculated using equation A-6:

$$EC = 2.8 \times 10^{-7} * \frac{VI}{Q} \quad (\text{A-6})$$

where  $V$  is potential obtained by LSV (V);  $I$  is the corresponding current (A);  $Q$  is volumetric flow rate of permeate (m<sup>3</sup> s<sup>-1</sup>);  $2.8 \times 10^{-7}$  is a conversion factor (kW s W<sup>-1</sup> h<sup>-1</sup>).

## REFERENCE

- (1) Buxton, G. V.; Greenstock, C. L.; Helman, W. P.; Ross, A. B., Critical-review of rate constants for reactions of hydrated electrons, hydrogen-atoms and hydroxyl radicals ( $\bullet\text{OH}/\bullet\text{O-}$ ) in aqueous-solution. *J. Phys. Chem. Ref. Data* **1988**, *17*, (2), 513-886.
- (2) Zaky, A. M.; Chaplin, B. P., Mechanism of p-substituted phenol oxidation at a  $\text{Ti}_4\text{O}_7$  reactive electrochemical membrane. *Environ. Sci. Technol.* **2014**, *48*, (10), 5857-5867.
- (3) Zaky, A. M.; Chaplin, B. P., Porous substoichiometric  $\text{TiO}_2$  anodes as reactive electrochemical membranes for water treatment. *Environ. Sci. Technol.* **2013**, *47*, (12), 6554-6563.
- (4) Li, X. X.; Zhu, A. L.; Qu, W.; Wang, H. J.; Hui, R.; Zhang, L.; Zhang, J. J., Magneli phase  $\text{Ti}_4\text{O}_7$  electrode for oxygen reduction reaction and its implication for zinc-air rechargeable batteries. *Electrochim. Acta.* **2010**, *55*, (20), 5891-5898.
- (5) Kundu, D.; Black, R.; Berg, E. J.; Nazar, L. F., A highly active nanostructured metallic oxide cathode for aprotic  $\text{Li-O}_2$  batteries. *Energy Environ. Sci.* **2015**, *8*, (4), 1292-1298.
- (6) Walsh, F. C.; Wills, R. G. A., The continuing development of Magneli phase titanium sub-oxides and Ebonex (R) electrodes. *Electrochim. Acta.* **2010**, *55*, (22), 6342-6351.
- (7) Krishnan, P.; Advani, S. G.; Prasad, A. K., Magneli phase  $\text{Ti}_n\text{O}_{2n-1}$  as corrosion-resistant PEM fuel cell catalyst support. *J. Solid State Electrochem.* **2012**, *16*, (7), 2515-2521.
- (8) Kim, K. M.; Kim, G. H.; Song, S. J.; Seok, J. Y.; Lee, M. H.; Yoon, J. H.; Hwang, C. S., Electrically configurable electroforming and bipolar resistive switching in  $\text{Pt/TiO}_2/\text{Pt}$  structures. *Nat. Nanotechnol.* **2010**, *21*, (30).
- (9) Knaup, J. M.; Marx, J.; Frauenheim, T., Reduction of the  $\text{TiO}_{2-x}$  melting temperature induced by oxygen deficiency with implications on experimental data accuracy and structural transition processes. *Phys. Status Solidi-R.* **2014**, *8*, (6), 549-553.
- (10) Toyoda, M.; Yano, T.; Tryba, B.; Mozia, S.; Tsumura, T.; Inagaki, M., Preparation of



carbon-coated Magneli phases  $Ti_nO_{2n-1}$  and their photocatalytic activity under visible light. *Appl. Catal., B* **2009**, 88, (1-2), 160-164.

(11) Smith, J. R.; Walsh, F. C.; Clarke, R. L., Reviews in applied electrochemistry. Number 50 - Electrodes based on Magneli phase titanium oxides: the properties and applications of Ebonex® materials. *J. Appl. Electrochem.* **1998**, 28, (10), 1021-1033.

(12) Chaplin, B. P., Critical review of electrochemical advanced oxidation processes for water treatment applications. *Environ. Sci. Process. Impacts* **2014**, 16, (6), 1182-1203.

(13) Chen, G.; Betterton, E. A.; Arnold, R. G.; Ela, W. P., Electrolytic reduction of trichloroethylene and chloroform at a Pt- or Pd-coated ceramic cathode. *J. Appl. Electrochem.* **2003**, 33, (2), 161-169.

(14) Kearney, D.; Bejan, D.; Bunce, N. J., The use of Ebonex® electrodes for the electrochemical removal of nitrate ion from water. *Can. J. Chem.* **2012**, 90, (8), 666-674.

(15) Hayfield, P., *Development of a new material: monolithic  $Ti_4O_7$  Ebonex® ceramic*. Royal Society of Chemistry: 2002.

(16) Zhang, Q. Y.; Vecitis, C. D., Conductive CNT-PVDF membrane for capacitive organic fouling reduction. *J. Membr. Sci.* **2014**, 459, 143-156.

(17) Dudchenko, A. V.; Rolf, J.; Russell, K.; Duan, W. Y.; Jassby, D., Organic fouling inhibition on electrically conducting carbon nanotube-polyvinyl alcohol composite ultrafiltration membranes. *J. Membr. Sci.* **2014**, 468, 1-10.

(18) Elmidaoui, A.; Elhannouni, F.; Sahli, M. A. M.; Chay, L.; Elabbassi, H.; Hafsi, M.; Largeteau, D., Pollution of nitrate in Moroccan ground water: removal by electrodialysis. *Desalination* **2001**, 136, (1-3), 325-332.

(19) Gusev, A. A.; Avvakumov, E. G.; Medvedev, A. Z.; Masliy, A. I., Ceramic electrodes based on magneli phases of titanium oxides. *Sci Sinter* **2007**, 39, (1), 51-57.

(20) Gusev, A. A.; Avvakumov, E. G.; Vinokurova, O. B., Synthesis of  $Ti_4O_7$  Magneli phase using mechanical activation. *Sci Sinter* **2003**, 35, (3), 141-145.

- (21) Tang, C.; Zhou, D. B.; Zhang, Q., Synthesis and characterization of Magneli phases: Reduction of  $\text{TiO}_2$  in a decomposed  $\text{NH}_3$  atmosphere. *Mater Lett* **2012**, 79, 42-44.
- (22) Kitada, A.; Hasegawa, G.; Kobayashi, Y.; Kanamori, K.; Nakanishi, K.; Kageyama, H., Selective preparation of macroporous monoliths of conductive titanium oxides  $\text{Ti}_n\text{O}_{2n-1}$  ( $n=2, 3, 4, 6$ ). *J Am Chem Soc* **2012**, 134, (26), 10894-10898.
- (23) Qian, S.; Mao, J., A practical and feasible way to synthesize Magneli phase conductive nanowires. *J Mater Sci-Mater El* **2015**, 26, (7), 5166-5169.
- (24) Comninellis, C.; Nerini, A., Anodic oxidation of phenol in the presence of NaCl for wastewater treatment. *J. Appl. Electrochem.* **1995**, 25, 23-28.
- (25) Sires, I.; Brillas, E.; Oturan, M. A.; Rodrigo, M. A.; Panizza, M., Electrochemical advanced oxidation processes: today and tomorrow. A review. *Environ Sci Pollut Res Int* **2014**, 21, (14), 8336-67.
- (26) Chong, M. N.; Sharma, A. K.; Burn, S.; Saint, C. P., Feasibility study on the application of advanced oxidation technologies for decentralised wastewater treatment. *Journal of Cleaner Production* **2012**, 35, 230-238.
- (27) Comninellis, C.; Kapalka, A.; Malato, S.; Parsons, S. A.; Poullos, I.; Mantzavinos, D., Advanced oxidation processes for water treatment: advances and trends for R&D. *Journal of Chemical Technology & Biotechnology* **2008**, 83, (6), 769-776.
- (28) Husain, S. R.; Cillard, J.; Cillard, P., Hydroxyl radical scavenging activity of flavonoids. *Phytochemistry* **1987**, 26, 2489-2491.
- (29) Comninellis, C., Electrocatalysis in the electrochemical conversion/combustion of organic pollutants for waste water treatment. *Electrochim. Acta.* **1993**, 39, 1857-1862.
- (30) USEPA Nitonal Primary Drinking Water Regulartions Home Page. <http://water.epa.gov/drink/contaminants/index.cfm>
- (31) Gherardini, L.; Michaud, P. A.; Panizza, M.; Comninellis, C.; Vatistas, N., Electrochemical oxidation of 4-chlorophenol for wastewater treatment. *J Electrochem Soc* **2001**, 148, D78-D82.

- (32) Sirés, I.; Low, C. T. J.; Ponce-de-León, C.; Walsh, F. C., The characterisation of PbO<sub>2</sub>-coated electrodes prepared from aqueous methanesulfonic acid under controlled deposition conditions. *Electrochim. Acta.* **2010**, *55*, (6), 2163-2172.
- (33) Chaplin, B. P.; Wyle, I.; Zeng, H.; Carlisle, J. A.; Farrell, J., Characterization of the performance and failure mechanisms of boron-doped ultrananocrystalline diamond electrodes. *J. Appl. Electrochem.* **2011**, *41*, (11), 1329-1340.
- (34) Widjaja, F. Titanium dioxide (TiO<sub>2</sub>) prices and pricing information. <http://www.icis.com/resources>
- (35) Bejan, D.; Guinea, E.; Bunce, N. J., On the nature of the hydroxyl radicals produced at boron-doped diamond and Ebonex® anodes. *Electrochim. Acta.* **2012**, *69*, 275-281.
- (36) Chen, G.; Bare, S. R.; Mallouk, T. E., Development of supported bifunctional electrocatalysts for unitized regenerative fuel cells. *J. Electroanal. Chem.* **2002**, *149*, (8), A1092-A1099.
- (37) Chen, G.; Waraksa, C. C.; Cho, H.; Macdonald, D. D.; Mallouk, T. E., EIS studies of porous oxygen electrodes with discrete particles. I. Impedance of oxide catalyst supports. *Journal of Electrochemical Society* **2003**, *140*, E423-E428.
- (38) EI-Sherif, S.; Bejan, D.; Bunce, N. J., Electrochemical oxidation of sulfide ion in synthetic sour brines using periodic polarity reversal at Ebonex® Electrode. *Can. J. Chem.* **2010**, *88*, (9).
- (39) Morris, D.; Dou, Y.; Rebane, J.; Mitchell, C. E. J.; Egdell, R. G.; Law, D. S. L.; Vittadini, A.; Casarin, M., Photoemission and STM study of the electronic structure of Nb-doped TiO<sub>2</sub>. *Physical Review B* **2000**, *61*, (20).
- (40) Zhang, Q.; Vecitis, C. D., Conductive CNT-PVDF membrane for capacitive organic fouling reduction. *J. Membr. Sci.* **2014**, *459*, 143-156.
- (41) Yamamura, H.; Kimura, K.; Watanabe, Y., Mechanism involved in the evolution of physically irreversible fouling in microfiltration and ultrafiltration membranes used for drinking water treatment. *Environ. Sci. Technol.* **2007**, *41*, 6789-6794.

- (42) Mierzwa, J. C.; da Silva, M. C. C.; Veras, L. R. V.; Subtil, E. L.; Rodrigues, R.; Li, T.; Landenberger, K. R., Enhancing spiral-wound ultrafiltration performance for direct drinking water treatment through operational procedures improvement: A feasible option for the Sao Paulo Metropolitan Region. *Desalination* **2012**, *307*, 68-75.
- (43) Rana, D.; Matsuura, T., Surface Modifications for Antifouling Membranes. *Chemical Review* **2010**, *110*, 2448-2471.
- (44) Mo, Y.; Tiraferri, A.; Yip, N. Y.; Adout, A.; Huang, X.; Elimelech, M., Improved antifouling properties of polyamide nanofiltration membranes by reducing the density of surface carboxyl groups. *Environ Sci Technol* **2012**, *46*, (24), 13253-61.
- (45) de Lannoy, C. F.; Jassby, D.; Davis, D. D.; Wiesner, M. R., A highly electrically conductive polymer–multiwalled carbon nanotube nanocomposite membrane. *J. Membr. Sci.* **2012**, *415-416*, 718-724.
- (46) H., L. I.; Moody, R. A., Electrically conductive membranes: synthesis and applications. *J. Membr. Sci.* **1990**, *50*, 31-49.
- (47) Ebbesen, T. W.; Lezec, H. J.; Hiurat, H.; Bennett, J. W.; Ghaemi, H. F.; Thio, T., Electrical conductivity of individual carbon nanotubes. *Nature* **1996**, 382.
- (48) Liu, Y.; Dustin Lee, J. H.; Xia, Q.; Ma, Y.; Yu, Y.; Lanry Yung, L. Y.; Xie, J.; Ong, C. N.; Vecitis, C. D.; Zhou, Z., A graphene-based electrochemical filter for water purification. *J. Mater. Chem. A* **2014**, *2*, (39), 16554-16562.
- (49) Gao, G.; Zhang, Q.; Hao, Z.; Vecitis, C. D., Carbon nanotube membrane stack for flow-through sequential regenerative electro-Fenton. *Environ Sci Technol* **2015**, *49*, (4), 2375-83.
- (50) Gao, G.; Zhang, Q.; Vecitis, C. D., CNT–PVDF composite flow-through electrode for single-pass sequential reduction–oxidation. *Journal of Materials Chemistry A* **2014**, *2*, (17), 6185.
- (51) Chaplin, B. P.; Roundy, E.; Guy, K. A.; Shapley, J. R.; Werth, C. J., Effects of natural water ions and humic acid on catalytic nitrate reduction kinetics using an alumina supported Pd-Cu catalyst. *Environ. Sci. Technol.* **2006**, *40*, 3075-3081.

(52) Schoeman, J. J.; Steyn, A., Nitrate removal with reverse osmosis in a rural area in South Africa. *Desalination* **2003**, *155*, (1), 15-26.

(53) Jensen, V. B.; Darby, J. L. *Drinking water treatment for nitrate-Technical report 6*; University of California, Davis  
California, USA., 2012.

(54) Samatya, S.; Kabay, N.; Yuksel, U.; Arda, M.; Yuksel, M., Removal of nitrate from aqueous solution by nitrate selective ion exchange resins. *React Funct Polym* **2006**, *66*, (11), 1206-1214.

(55) Katsounaros, I.; Ipsakis, D.; Polatides, C.; Kyriacou, G., Efficient electrochemical reduction of nitrate to nitrogen on tin cathode at very high cathodic potentials. *Electrochim. Acta*. **2006**, *52*, (3), 1329-1338.

(56) Bouzek, K.; Paidar, M.; Sadilkova, A.; Bergmann, H., Electrochemical reduction of nitrate in weakly alkaline solutions. *J. Appl. Electrochem.* **2001**, *31*, 1185-1193.

(57) Li, M.; Feng, C.; Zhang, Z.; Shen, Z.; Sugiura, N., Electrochemical reduction of nitrate using various anodes and a Cu/Zn cathode. *Electrochem. Commun.* **2009**, *11*, (10), 1853-1856.

(58) polatides, C.; Kyriacou, G., Electrochemical reduction of nitrate ion on various cathodes- reaction kinetics on bronze cathode. *J. Appl. Electrochem.* **2005**, *35*, 421-427.

(59) Comisso, N.; Cattarin, S.; Fiameni, S.; Gerbasi, R.; Mattarozzi, L.; Musiani, M.; Vázquez-Gómez, L.; Verlato, E., Electrodeposition of Cu–Rh alloys and their use as cathodes for nitrate reduction. *Electrochem. Commun.* **2012**, *25*, 91-93.

(60) Ureta-Zanartu, M. S.; Yanez, C.; Reyes, G.; Gancedo, J. R.; Marco, J. F., Electrodeposited Pt-Ir electrodes: characterization and electrocatalytic activity for the reduction of the nitrate ion. *J Solid State Electrochem* **1998**, *2*, 191-197.

(61) Kim, K.; Kim, S.; Kim, Y.; Lee, E.; Shin, D.; Song, K., Platinization of Ti for the fabrication of a Sn-modified Pt/Ti electrode for reduction of nitrate. *J. Appl. Electrochem.* **2008**, *38*, 1535-1543.

(62) Figueiredo, M. C.; Souza-Garcia, J.; Climent, V.; Feliu, J. M., Nitrate reduction on Pt(111) surfaces modified by Bi adatoms. *Electrochem. Commun.* **2009**, *11*, (9), 1760-1763.

(63) Keita, B.; Abdeljalil, E.; Nadjo, L.; Contant, R.; Belgiche, R., First examples of efficient participation of selected metal-ion-substituted heteropolyanions in electrocatalytic nitrate reduction. *Electrochem. Commun.* **2001**, *3*, 56-62.

(64) Matsushima, J. T.; Fernandes, V. C.; Couto, A. B.; Baldan, M. R.; Ferreira, N. G., Investigation of a Cu/Pd bimetallic system electrodeposited on boron-doped diamond films for application in electrocatalytic reduction of nitrate. *International Journal of Electrochemistry* **2011**, 2012.

(65) Giesting, P.; Guggenheim, S.; van Groos, A. F. K.; Busch, A., X-ray diffraction study of K- and Ca-exchanged montmorillonites in CO<sub>2</sub> atmospheres. *Environ. Sci. Technol.* **2012**, *46*, (10), 5623-5630.

(66) Jing, Y.; Guo, L.; Chaplin, B. P., Electrochemical impedance spectroscopy study of reactive electrochemical membrane fouling and development of a new regeneration scheme. *J. Membr. Sci.* **Under Review**.

(67) Shain, I.; Nicholson, R. S., Citation classic - theory of stationary electrode polarography - single scan and cyclic methods applied to reversible, irreversible, and kinetic systems. *CCPCE* **1981**, (6), 18-18.

(68) YaP, G., General equations of oscillographic polarography, reversible processes at the cathodic and anodic polarisation. *Dokl Akad Nauk SSSR* **1959**.

(69) Aouina, N.; Cachet, H.; Debiemme-chouvy, C.; Thi, T. M. T., Insight into the electroreduction of nitrate ions at a copper electrode, in neutral solution, after determination of their diffusion coefficient by electrochemical impedance spectroscopy. *Electrochim. Acta.* **2010**, *55*, (24), 7341-7345.

(70) Heil, S. R.; Holz, M.; Kastner, T. M.; Weingartner, H., Self-diffusion of the perchlorate ion in aqueous-electrolyte solutions measured by Cl-35 Nmr Spin-Echo experiments. *J. Chem. Soc., Faraday Trans.* **1995**, *91*, (12), 1877-1880.

(71) Chen, G.; Betterton, E. A.; Arnold, R. G., Electrolytic oxidation of trichloroethylene

using a ceramic anode. *J. Appl. Electrochem.* **1999**, 29, (8), 961-970.

(72) Ferro, S.; Martinez-Huitle, C. A.; De Battisti, A., Electrooxidation of oxalic acid at different electrode materials. *J. Appl. Electrochem.* **2010**, 40, (10), 1779-1787.

(73) Garcia-Segura, S.; Brillas, E., Mineralization of the recalcitrant oxalic and oxamic acids by electrochemical advanced oxidation processes using a boron-doped diamond anode. *Water Res.* **2011**, 45, (9), 2975-2984.

(74) Donaghue, A.; Chaplin, B. P., Effect of select organic compounds on perchlorate formation at boron-doped diamond film anodes. *Environ. Sci. Technol.* **2013**, 47, (21), 12391-12399.

(75) Ishibashi, K.; Fujishima, A.; Watanabe, T.; Hashimoto, K., Detection of active oxidative species in TiO<sub>2</sub> photocatalysis using the fluorescence technique. *Electrochem. Commun.* **2000**, 2, (3), 207-210.

(76) Singh, T. S.; Rao, B. S. M.; Mohan, H.; Mittal, J. P., A pulse radiolysis study of coumarin and its derivatives. *J. Photochem. Photobiol., A* **2002**, 153, (1-3), 163-171.

(77) Charbouillot, T.; Brigante, M.; Mailhot, G.; Maddigapu, P. R.; Minero, C.; Vione, D., Performance and selectivity of the terephthalic acid probe for (OH)-O-center dot as a function of temperature, pH and composition of atmospherically relevant aqueous media. *J. Photochem. Photobiol., A* **2011**, 222, (1), 70-76.

(78) Iniesta, J.; Michaud, P. A.; Panizza, M.; Cerisola, G.; Aldaz, A.; Comninellis, C., Electrochemical oxidation of phenol at boron-doped diamond electrode. *Electrochim. Acta.* **2001**, 46, (23), 3573-3578.

(79) Mishra, D.; Liao, Z. H.; Farrell, J., Understanding reductive dechlorination of trichloroethene on boron-doped diamond film electrodes. *Environ. Sci. Technol.* **2008**, 42, (24), 9344-9349.

(80) Jurczakowski, R.; Hitz, C.; Lasia, A., Impedance of porous Au based electrodes. *J. Electroanal. Chem.* **2004**, 572, (2), 355-366.

(81) Yang, J.; Wang, J.; Jia, J. P., Improvement of electrochemical wastewater treatment

through mass transfer in a seepage carbon nanotube electrode reactor. *Environ. Sci. Technol.* **2009**, *43*, (10), 3796-3802.

(82) Tsierkezos, N. G.; Ritter, U., Electrochemical and thermodynamic properties of hexacyanoferrate(II)/(III) redox system on multi-walled carbon nanotubes. *J. Chem. Thermodyn.* **2012**, *54*, 35-40.

(83) Schnoor, M. H.; Vecitis, C. D., Quantitative examination of aqueous ferrocyanide oxidation in a carbon nanotube electrochemical filter: effects of flow rate, ionic strength, and cathode material. *J. Phys. Chem. C* **2013**, *117*, (6), 2855-2867.

(84) Louit, G.; Foley, S.; Cabillic, J.; Coffigny, H.; Taran, F.; Valleix, A.; Renault, J. P.; Pin, S., The reaction of coumarin with the OH radical revisited: hydroxylation product analysis determined by fluorescence and chromatography. *Radia. Phys. Chem.* **2005**, *72*, (2-3), 119-124.

(85) Rueffer, M.; Bejan, D.; Bunce, N. J., Graphite: An active or an inactive anode? *Electrochim. Acta.* **2011**, *56*, (5), 2246-2253.

(86) Terashima, C.; Rao, T. N.; Sarada, B. V.; Tryk, D. A.; Fujishima, A., Electrochemical oxidation of chlorophenols at a boron-doped diamond electrode and their determination by high-performance liquid chromatography with amperometric detection. *Anal. Chem.* **2002**, *74*, (4), 895-902.

(87) Hayashi, T.; Sakurada, I.; Honda, K.; Motohashi, S.; Uchikura, K., Electrochemical detection of sugar-related compounds using boron-doped diamond electrodes. *Anal. Sci.* **2012**, *28*, (2), 127-133.

(88) Komatsu, M.; Rao, T. N.; Fujishima, A., Detection of hydroxyl radicals formed on an anodically polarized diamond electrode surface in aqueous media. *Chem. Lett.* **2003**, *32*, (4), 396-397.

(89) Farrell, J.; Martin, F. J.; Martin, H. B.; O'Grady, W. E.; Natishan, P., Anodically generated short-lived species on boron-doped diamond film electrodes. *J Electrochem Soc* **2005**, *152*, (1), E14-E17.

(90) Kapalka, A.; Foti, G.; Comninellis, C., The importance of electrode material in



environmental electrochemistry Formation and reactivity of free hydroxyl radicals on boron-doped diamond electrodes. *Electrochim. Acta.* **2009**, *54*, (7), 2018-2023.

(91) Bi, J. J.; Peng, C. S.; Xu, H. Z.; Ahmed, A. S., Removal of nitrate from groundwater using the technology of electrodialysis and electrodeionization. *Desalination Water Treat.* **2011**, *34*, (1-3), 394-401.

(92) Ren, H. Y.; Wang, Q.; Zhang, X. Y.; Kang, R. J.; Shi, S. Y.; Cong, W., Membrane fouling caused by amino acid and calcium during bipolar membrane electrodialysis. *J. Chem. Technol. Biotechnol.* **2008**, *83*, (11), 1551-1557.

(93) Lee, H. J.; Choi, J. H.; Cho, J. W.; Moon, S. H., Characterization of anion exchange membranes fouled with humate during electrodialysis. *J. Membr. Sci.* **2002**, *203*, (1-2), 115-126.

(94) Lee, H. J.; Hong, M. K.; Han, S. D.; Cho, S. H.; Moon, S. H., Fouling of an anion exchange membrane in the electrodialysis desalination process in the presence of organic foulants. *Desalination* **2009**, *238*, (1-3), 60-69.

(95) Lee, H. J.; Hong, M. K.; Han, S. D.; Shim, J.; Moon, S. H., Analysis of fouling potential in the electrodialysis process in the presence of an anionic surfactant foulant. *J. Membr. Sci.* **2008**, *325*, (2), 719-726.

(96) Epron, F.; Gauthard, F.; Pineda, C.; Barbier, J., Catalytic reduction of nitrate and nitrite on Pt-Cu/Al<sub>2</sub>O<sub>3</sub>, Catalysts in aqueous solution: role of the interaction between copper and platinum in the reaction. *Journal of Catalysis* **2001**, *198*, (2), 309-318.

(97) Gauthard, F.; Epron, F.; Barbier, J., Palladium and platinum-based catalysts in the catalytic reduction of nitrate in water : effect of copper, silver, or gold addition. *Journal of Catalysis* **2003**, *220*, (1), 182-191.

(98) Badea, G. E., Electrocatalytic reduction of nitrate on copper electrode in alkaline solution. *Electrochim. Acta.* **2009**, *54*, (3), 996-1001.

(99) Kerkeni, S.; Lamy-Pitara, E.; Barbier, J., Copper-platinum catalysts prepared and characterized by electrochemical methods for the reduction of the nitrate and nitrite. *Catalysis Today* **2002**, *75*, 35-42.

---

(100) Brug, G. J.; Vandeneeden, A. L. G.; Sluytersrehabach, M.; Sluyters, J. H., The Analysis of electrode impedances complicated by the presence of a constant phase element. *J. Electroanal. Chem.* **1984**, 176, (1-2), 275-295.

(101) Levine, S.; Smith, A. L., Theory of differential capacity of oxide-aqueous electrolyte interface. *Discuss. Faraday Soc.* **1971**, (52), 290-301.

(102) Bard, A. J.; Faulkner, L. R., *Electrochemical Methods: Fundamentals and Applications*. John Wiley & Sons, INC.: 2001.

## VITA

**NAME:** Lun Guo

**Email:** [guolun.umich@gmail.com](mailto:guolun.umich@gmail.com)

### EDUCATION

---

<b>University of Illinois at Chicago (UIC), Illinois, USA</b>	<b>2013 –2015</b>
College of Chemical Engineering, MS.	
<b>University of Michigan (UM), Ann Arbor, USA</b>	<b>2010 –2012</b>
College of Chemical Engineering, Bachelor	
<b>Shanghai Jiao Tong University (SJTU), Shanghai, China</b>	<b>2008 –2013</b>
College of Electrical & Computer Science Engineering, Bachelor	

### EXPERIENCE

#### Development and Characterization of Ultrafiltration Reactive Electrochemical Membrane

*Research Assistant in Brian P. Chaplin's Wastewater Treatment Group in UIC*

Synthesized and characterized a novel ceramic membrane made of TiO<sub>2</sub> Magnéli phase. Tested the disinfection effect of Magnéli phase membrane with E. coli bacteria. Submitted two peer-reviewed publications in well-recognized scientific journals.

#### Teacher Assistant of Numerical Methods for Chemical Engineering

*Graduate Teacher Assistant*

Assisted the instructor in preparing and grading exams and homework in ChE 205.

#### Water Vaporization Modeling using CFD Techniques

*Research Assistant in GE of Shanghai*

Worked on development of model for water vaporization using CFD. Elected as conferred Outstanding Researcher Award by GE Global Research Center.

#### Development of Catheter Sterilization Operations using CFD Techniques

*Research Assistant in Medical School in UM, Ann Arbor*

Developed a technique for central venous catheter sterilization with CFD modeling.

#### Monte Carlo Method Simulation of Particle Aggregation under Depletion Potential

*Research Assistant in Prof. Michael J. Solomon in UM, Ann Arbor*

Completed independent project guided by graduate student Lilian Hsiao in Prof. Michael Solomon's group.

Completed a program to simulate aggregation of particles under depletion potential. Worked in Prof.

Michael J. Solomon's lab to synthesize micron level particles guided by Lilian.

### HONORS AND AWARDS

---

UM-SJTU Joint Institute Dean's List	<b>2008 &amp;2010</b>
Chemical Engineering of University of Michigan Dean's List	<b>2013</b>

### PUBLICATIONS

1. Lun, Guo; Chaplin, Brian P., Development and Characterization of Ultrafiltration TiO<sub>2</sub> Magnéli Phase Reactive Electrochemical Membranes. *Environmental Science and Technology*, Submitted.
2. Lun Guo; Kai Ding; Karl Rockne; Metin Duran; Brian P. Chaplin. *Journal of Hazardous Materials*. Submitted
3. Yin, Jing; Lun, Guo; Chaplin, Brian P., Electrochemical Impedance Spectroscopy Study of Reactive Electrochemical Membrane Fouling and Development of a New Regeneration Scheme. *Journal of Membrane Science*, Submitted.